

FORMING EARLY-TYPE GALAXIES IN Λ CDM SIMULATIONS -I. ASSEMBLY HISTORIES

PETER H. JOHANSSON^{1,2}, THORSTEN NAAB³, JEREMIAH P. OSTRIKER⁴

¹ Department of Physics, University of Helsinki, Gustaf Hällströmin katu 2a, FI-00014 Helsinki, Finland Peter.Johansson@helsinki.fi

² Finnish Centre for Astronomy with ESO, University of Turku, Väisäläntie 20, FI-21500 Piikkiö, Finland

³ Max-Planck-Institut für Astrophysik, Karl-Schwarzschild-Str. 1, D-85741, Garching bei München, Germany

⁴ Department of Astrophysics, Peyton Hall, Princeton, NJ 08544, USA

Draft version November 12, 2018

ABSTRACT

We present a sample of nine high resolution cosmological simulations in the mass range of $M_{\text{vir}} = 7 \times 10^{11} - 4 \times 10^{12} M_{\odot}$ starting from Λ CDM initial conditions. Our simulations include primordial radiative cooling, photoionization, star formation, supernova II feedback, but exclude supernova driven winds and AGN feedback. The simulated galaxies assemble in two phases, with the initial growth dominated by compact ($r < r_{\text{eff}}$) in situ star formation fueled by cold, low entropy gas streams resulting in a very similar mean assembly redshift of $z_{f,\text{ins}} \sim 2.5$ for the in situ stellar component in all galaxies. The late growth is dominated by accretion of old stars formed in subunits outside the main galaxy ($r > r_{\text{eff}}$) resulting in an assembly redshift of $z_{f,\text{acc}} \sim 0.5 - 1.5$ with much larger scatter. We find a positive correlation between the fraction of accreted stars and the final mass of our galaxies. We show that gravitational feedback strongly suppresses late star formation in massive galaxies contributing to the observed galaxy color bimodality. The accretion of stellar material is also responsible for the observed size growth of early-type galaxies. In addition, we find that the dark matter fractions within the stellar half-mass radii continuously increase towards lower redshift from about $f_{\text{DM}} \sim 0.05$ at $z \sim 3$ to $f_{\text{DM}} \sim 0.1 - 0.3$ at $z = 0$. Furthermore, the logarithmic slope of the total density profile is nearly isothermal at the present-day ($\gamma' \sim 1.9 - 2.2$). Finally, the input of gravitational heating lowers the central dark matter densities in the galaxies, with the effect being smaller compared to simulations without supernova feedback.

Subject headings: cosmology: theory — galaxies: elliptical and lenticular, cD — galaxies: formation — galaxies: evolution — methods: numerical

1. INTRODUCTION

In the classic cold dark matter (CDM) picture of galaxy formation, gas falling into dark matter halos is shock-heated approximately to the halo virial temperature, $T_{\text{vir}} = 10^6 (v_{\text{circ}}/167 \text{ km s}^{-1})^2$ K maintaining quasi-hydrostatic equilibrium with the dark matter component (Rees & Ostriker 1977; Silk 1977; White & Rees 1978). Then, given a density-profile for the gas, a cooling radius can be calculated, inside of which the gas can radiate its thermal energy away, losing its pressure support, and settling into a centrifugally supported disk while conserving its specific angular momentum (Fall & Efstathiou 1980). Eventually the collapsing gas reaches high enough densities to allow for star formation and a stellar disk is grown from the inside out. Over the years this simplified picture has been updated and extended into the powerful framework of semi-analytic galaxy formation (e.g. White & Frenk 1991; Kauffmann et al. 1993; Cole et al. 2000; De Lucia et al. 2006; Somerville et al. 2008) that has been successful in reproducing many of the present-day properties of observed galaxies.

A first challenge of the standard model of galaxy formation was already brought up by Binney (1977), who used analytical models of protogalactic collapse to argue that under some plausible physical conditions the fraction of shock-heated gas could be small with the majority of the gas having temperatures below T_{vir} . This idea was revived by Birnboim & Dekel (2003); Dekel & Birnboim (2006), who assuming spherical symmetry showed that

galaxy halos can only shock-heat infalling gas if the cooling rate for gas behind the shock is lower than the compression rate of the infalling gas. This criterion translates to a critical minimum mass for halos that are able to shock-heat the infalling gas of $M_{\text{shock}} \approx 10^{11.6} M_{\odot}$, with this mass being roughly independent of redshift and very similar to the critical mass isolated already in the papers by Rees & Ostriker (1977) and Silk (1977). Halos below this mass are not massive enough to support stable shocks and the majority of their gas is accreted cold. However, galaxies above the critical shock mass can also be fed with cold gas along filaments penetrating deep inside the hot halo. This general picture has since been confirmed in cosmological simulations using both Smoothed Particle Hydrodynamics (SPH) (Kereš et al. 2005, 2009; Brooks et al. 2009) and Adaptive Mesh Refinement (AMR) (Ocvirk et al. 2008) techniques.

Since the early days of galaxy studies it has been clear that the majority of galaxies come in two types, either as early-type elliptical galaxies or late-type spiral disk galaxies as manifested in the classical Hubble sequence (Hubble 1926). Several recent large statistical surveys of the local galaxy population, such as the Sloan Digital Sky Survey (SDSS) and the two-degree Field (2df) surveys, have made this bimodality even more robust. (e.g. Bell et al. 2003; Kauffmann et al. 2003; Baldry et al. 2004). The division between the two classes of galaxies is associated with a critical stellar mass of $M_{\text{crit}} \simeq 3 \times 10^{10} M_{\odot}$. Galaxies below this critical mass are typically blue, star-forming disk galaxies that lie in

the field, whereas galaxies above M_{crit} are dominated by red spheroidal systems with old stellar populations that can be found both in overdense regions and in the field.

Due to the inherent complexity and non-linearity of the galaxy formation process, numerical computer simulations have become the ideal tool for studying structure formation. Interestingly, most numerical studies starting from cosmological initial conditions have concentrated on the formation of late-type Milky Way-like galaxies (e.g. Sommer-Larsen et al. 2003; Robertson et al. 2004; Governato et al. 2004, 2007; Scannapieco et al. 2009; Agertz et al. 2009; Piontek & Steinmetz 2011; Agertz et al. 2011). Much less effort has been spent on studying elliptical galaxies (Meza et al. 2003; Naab et al. 2007, hereafter N07; Feldmann et al. 2010) which is somewhat surprising as they contain a significant fraction of the stars in the Universe (Fukugita et al. 1998; Driver et al. 2007) with the most massive galaxies known all being spheroidal systems (e.g. Thomas et al. 2005; Kormendy et al. 2009).

However, a proposed formation mechanism of elliptical galaxies that has been studied extensively is the binary merger scenario, in which elliptical galaxies are formed from the merger of two spiral galaxies. This picture is moderately successful in producing the component of intermediate mass, fast-rotating disk ellipticals with anisotropic velocity distributions. (e.g. Barnes & Hernquist 1996; Springel 2000; Bournaud et al. 2005; Naab et al. 2006a; Cappellari et al. 2007; Hopkins et al. 2008b; Hoffman et al. 2009; Bois et al. 2011; Cappellari et al. 2011; Emsellem et al. 2011; Krajnović et al. 2011). However, the binary merger scenario has problems in reproducing the massive old metal-rich slowly-rotating boxy ellipticals, which are characterized by low ellipticities and more isotropic velocities (Naab & Burkert 2003; Cox et al. 2006; Hopkins et al. 2008a; Naab & Ostriker 2009; Bois et al. 2010). The massive slowly rotating ellipticals are better reproduced in simulations set in the cosmological context, in which the galaxy is assembled from multiple, hierarchical mergers of starbursting subunits. (Burkert et al. 2008; Naab et al. 2009; Johansson et al. 2009c, hereafter J09; Oser et al. 2010; Feldmann et al. 2011; Oser et al. 2012).

Since the growth of structure in the CDM model is hierarchical, a naive reading of the model implies that the most massive galaxies residing in the most massive halos would form last. However, two recent key observational results have challenged this notion. Firstly, there is now very strong observational evidence that old, massive red metal-rich galaxies were already in place at redshifts of $z=2-3$ (e.g. Brinchmann & Ellis 2000; van der Wel et al. 2005). This result can also be seen as a manifestation of cosmic downsizing, in which the most massive galaxies formed a significant proportion of their stars at high redshifts, compared to the lower mass systems that have been forming stars over the whole cosmic epoch (e.g. Glazebrook et al. 2004; Juneau et al. 2005; Bundy et al. 2006; Cimatti et al. 2006). Secondly, there now also exists observational evidence for significant growth in both the size (e.g. Daddi et al. 2005; Trujillo et al. 2006, 2007; van Dokkum et al. 2008; van der Wel et al. 2009; van Dokkum et al. 2010) and mass (e.g. Bell et al. 2004; Drory et al. 2004; Faber et al. 2007) of massive ellipti-

cals since $z=2-3$ until the present-day. The observed $z \sim 2$ ellipticals are also typically an order of magnitude denser than their local counterparts and would need, in the absence of mergers, to undergo significant secular and internal evolution since $z \sim 2$ in order to match the local galaxy population (e.g. Cimatti et al. 2008; van Dokkum et al. 2008, 2009; Bezanson et al. 2009).

Theoretically, the observed bimodality in the galaxy distribution can be explained if star formation in halos above a critical threshold mass of $M \sim 10^{12} M_{\odot}$ is suppressed (e.g. Bower et al. 2006; Cattaneo et al. 2006). The quenching mechanism needs to be both energetic enough to trigger the quenching and long-lasting enough to maintain the quenching over a Hubble time. In addition to the quenching by shock-heated gas above a critical halo mass (Dekel & Birnboim 2006; Birnboim et al. 2007), potential quenching mechanisms include the feedback from AGNs (Ciotti & Ostriker 2007), gaseous major mergers triggering starburst and/or quasar activity (e.g. Mihos & Hernquist 1994, 1996; Springel et al. 2005; Naab et al. 2006a; Bower et al. 2006; Croton et al. 2006; Hopkins et al. 2007; Johansson et al. 2009b,a) and gravitational quenching by clumpy accretion (Khochfar & Ostriker 2008; Dekel & Birnboim 2008; Birnboim & Dekel 2011; J09).

In order to explain downsizing, the stars incorporated in massive galaxies need to form rapidly at high redshifts. This process could then proceed through the merging of multiple starbursting subunits, with star formation being potentially efficiently fueled by cold gas accretion (Dekel et al. 2009a). In some respect this scenario bears an uncanny resemblance to the monolithic collapse picture (Eggen et al. 1962; Larson 1975; van Albada 1982). After the rapid initial dissipational formation process the star formation is terminated already at redshifts $z=2-3$. The subsequent late assembly phase of the galaxy then proceeds through minor dry (gas-poor) merging (e.g. van Dokkum 2005; Naab et al. 2006b; Bell et al. 2006; Khochfar & Silk 2009; Hopkins et al. 2009, 2010), which would explain the growth in mass and size and the reduction in the central density (Naab et al. 2009; Bezanson et al. 2009; van der Wel et al. 2009; Oser et al. 2010, 2012). Furthermore, growth by dry merging does not violate stringent constraints on the galaxy colors and amount of young stars in massive ellipticals (Bell et al. 2004; Faber et al. 2007).

In this first paper (Paper I) building on previous work of N07; J09; Naab et al. (2009) we explore in more detail the cosmological formation of massive ellipticals using high-resolution numerical simulations to determine if the two phase picture provides a useful interpretation (see also Oser et al. 2010). We expand on our previous simulation sample by including a total of 9 galaxies simulated using cooling, star formation and feedback from type II supernovae. In agreement with our earlier studies we find that the simulated galaxies do assemble in two phases: The initial growth is dominated by compact ($r < r_{\text{eff}}$) in situ star formation fueled by cold gas flows, whereas the late growth is dominated by accretion of stars formed in subunits outside the main galaxy. The accreted stars assemble predominantly at larger radii ($r > r_{\text{eff}}$) explaining both the size and mass growth of the simulated galaxies in broad agreement with the observations. In a companion paper (Paper II Johansson et al.

TABLE 1
GALAXY PROPERTIES AT $r < r_{\text{vir}}$ AT $z = 0$.

Galaxy	$M_{\text{vir}}^{(a)}$	$M_*^{(a)}$	$M_{\text{gas}}^{(a)}$	$M_{\text{DM}}^{(a)}$	$z_{\text{f,DM}}^{(b)}$	$\Delta_{\text{DM}}^{(c)}$	$r_{\text{vir}}^{(d)}$	$v_{\text{max}}^{(e)}$	$\langle \lambda' \rangle^{(f)}$	$f_{\text{hot}}^{(g)}$	$m_*^{(h)}$	$m_{\text{DM}}^{(h)}$	$\epsilon_*^{(i)}$
C2	153.5	19.8	9.6	124.1	1.3	3.57	250	376	0.035	0.98	1.07	8.6	0.125
U	442.0	46.7	37.6	357.7	1.5	7.92	356	447	0.038	0.99	29	232	0.25
Y	219.0	24.2	17.0	177.8	0.8	4.72	281	405	0.056	0.98	46	368	0.25
A2	185.2	22.0	9.4	153.8	1.5	3.84	266	383	0.021	0.98	1.29	10.3	0.125
Q	90.7	11.5	5.9	73.3	1.6	1.74	210	298	0.056	0.89	8.5	69	0.25
T	136.7	14.0	7.3	115.4	1.5	2.62	241	310	0.050	0.99	8.5	69	0.25
E2	136.4	17.1	9.4	109.9	1.6	2.94	240	376	0.047	0.97	1.07	8.6	0.125
L	78.6	9.1	5.7	63.8	1.7	2.16	200	304	0.030	0.93	8.5	69	0.25
M	79.7	11.9	5.5	62.3	0.7	2.14	201	305	0.065	0.68	6.0	46	0.25

NOTE. — (a) Total masses M in $10^{10} M_{\odot}$; (b) Redshift at which half of the final DM component was assembled; (c) Overdensity of DM within a sphere of radius $r = 2$ Mpc, $\rho_{\text{DM}}(r < 2\text{Mpc}) / \langle \rho_{\text{DM}} \rangle$ (d) Virial radius in kpc, defined as the radius enclosing an overdensity of 200 times the critical density ρ_{crit} ; (e) Maximum total circular velocity in km/s; (f) Time-averaged halo spin parameter; (g) Fraction of hot gas ($T > 2.5 \times 10^5$ K); (h) Particle masses m in $10^5 M_{\odot}$; (i) Gravitational softening lengths in physical kpc, $\epsilon_{\text{DM}} = 2 \times \epsilon_*$

TABLE 2
GALAXY PROPERTIES AT $r < r_{\text{gal}}$ AT $z = 0$.

Galaxy	$M_*^{(a)}$	$f_{\text{acc}}^{(b)}$	$f_{\text{ins}}^{(b)}$	$z_{\text{f,*}}^{(c)}$	$M_{\text{gas}}^{(a)}$	$f_{\text{h}}^{(d)}$	$r_p^{(e)}$	$r_{3D}^{(f)}$	$\text{age}_*^{(g)}$	$f_{\text{conv}}^{(h)}$	$f_{\text{DM}}^{(i)}$	SFR ^(j)	SSFR ^(k)	Q/SF ^(l)
C2	14.0	0.73	0.27	1.0	0.18	0.96	2.05	2.71	11.2	0.56	0.11	0.3	-11.6	Q
U	25.1	0.81	0.19	1.4	1.78	1.00	3.11	4.16	11.6	0.35	0.20	3.5	-10.9	Q
Y	15.5	0.70	0.30	1.1	1.11	0.87	2.59	3.40	11.4	0.44	0.29	2.2	-10.8	Q
A2	15.1	0.56	0.44	1.6	0.17	0.83	2.36	3.19	11.3	0.49	0.19	0.4	-11.6	Q
Q	8.44	0.64	0.36	1.9	0.35	0.27	1.94	2.53	11.2	0.58	0.15	0.6	-11.2	Q
T	11.1	0.56	0.44	1.6	0.31	0.92	2.44	3.23	11.7	0.48	0.20	0.3	-11.6	Q
E2	11.2	0.64	0.34	1.6	0.18	0.90	1.49	1.93	11.4	0.51	0.08	0.3	-11.5	Q
L	7.00	0.35	0.65	2.5	0.34	0.99	1.57	2.02	11.4	0.54	0.18	0.9	-10.9	Q
M	8.37	0.61	0.39	0.9	0.24	0.12	1.69	2.20	10.6	0.67	0.12	0.6	-11.2	Q

NOTE. — (a) Total masses M in $10^{10} M_{\odot}$; (b) Fraction of accreted and in situ formed stars; (c) Redshift at which half of the final stellar component was assembled; (d) Fraction of hot gas ($T > 2.5 \times 10^5$ K); (e) Projected stellar half-mass radius in kpc; (f) 3D stellar half-mass radius in kpc; (g) Average stellar age in Gyr; (h) Baryon conversion factor; (i) Fraction of dark matter within r_{3D} ; (j) Mean star formation rate in M_{\odot}/yr averaged over the last 1 Gyr; (k) Logarithm of the specific star formation rate SFR/M_* in yr^{-1} ; (l) Classification of galaxy into quiescent (Q) or star-forming (SF) based on the SSFR

in prep) we study the photometric and kinematic properties of our simulated galaxies and perform a detailed comparison between the simulations and recent observations.

This paper is structured as follows. In §2 we discuss the numerical code, simulation physics and parameters employed in this study. We begin §3 by discussing the assembly history of the dark matter and stellar components of the simulated galaxies. We then continue by discussing the size evolution and dark matter fractions of the galaxies as a function of their assembly histories. In §4 we discuss the thermal history of the gas component in our simulated galaxies. Here we also demonstrate the importance of cold flows in the early assembly history of the galaxies and discuss the relative importance of supernova and gravitational feedback as a heating source. Finally, we summarize and discuss our findings in §5.

2. SIMULATIONS

2.1. Numerical code

The simulations presented in this paper were performed using the parallel TreeSPH-code GADGET-2 (Springel 2005). The code follows the gas dynamics using the Lagrangian Smoothed Particle Hydrodynamics (SPH) (e.g. Monaghan 1992) technique formulated in such a way that energy and entropy is manifestly conserved (Springel & Hernquist 2002). The code includes star formation and radiative cooling for a primordial mixture of hydrogen and helium, with the rates

computed assuming that the gas is optically thin and in ionization equilibrium (Katz et al. 1996). We included a spatially uniform redshift-dependent UV background radiation field with a modified Haardt & Madau (1996) spectrum, where reionization takes place at $z \simeq 6$ (Davé et al. 1999) and the UV background field peaks at $z \simeq 2 - 3$. For a detailed investigation on the effects of varying the background radiation field on the evolution of the galaxies presented in this paper, see Hambrick et al. (2009, 2011a).

For the simulations presented in N07;J09 we turned off the feedback from supernovae by eliminating the two-phase description of the ISM of star-forming particles in order to better understand galactic evolution in the absence of any energetic feedback from non-gravitational sources. However, in the study presented in this paper we include the full self-regulated supernova feedback model of Springel & Hernquist (2003) in all our simulations. In this model the ISM is treated as a two-phase medium (McKee & Ostriker 1977; Johansson & Efstathiou 2006) in which cold clouds are embedded in a tenuous hot gas at pressure equilibrium. Stars form from the cold clouds in regions where $n > n_{\text{th}} = 0.205 \text{ cm}^{-3}$ with the short-lived stars supplying an energy of 10^{51} ergs to the surrounding gas by supernovae. The threshold density, n_{th} , is determined self-consistently in the model by requiring that the equation-of-state (EOS) is continuous at the onset of star formation. The star formation rate in this model is set by $dp_*/dt = (1 - \beta)\rho_c/t_*$, where β is the mass fraction of

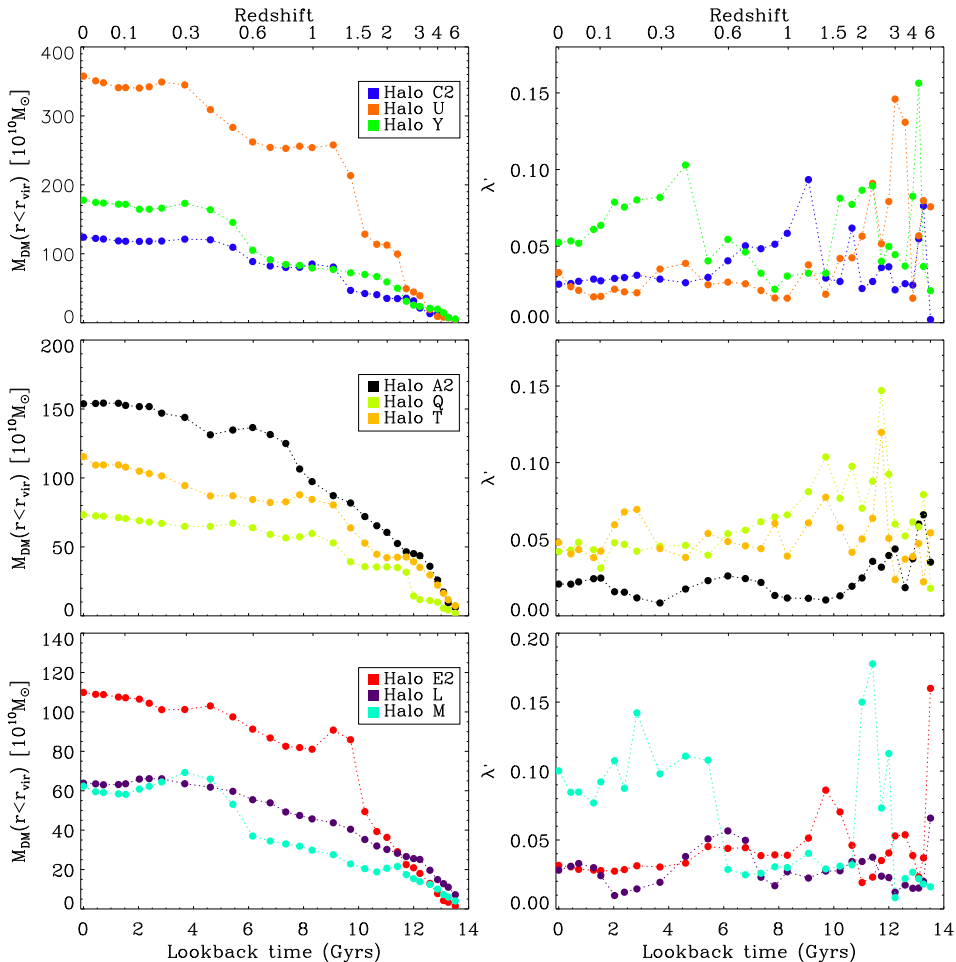


FIG. 1.— Dark matter mass accretion histories within the galaxy virial radii (left panels), together with the evolution of the halo spin parameter λ' (right panels) for the full galaxy sample. Major mergers can be seen as sudden increases in both the virial DM mass and the halo spin parameter. With the exception of halo M all galaxies have a relatively smooth accretion histories for the last 5 Gyrs.

massive stars ($> 8M_{\odot}$), ρ_c is density of cold gas and t_* is the star formation time scale set by $t_* = t_*^0(n/n_{\text{th}})^{-1/2}$. Each gas particle can produce a maximum of two stellar particles per particle, with the resulting stellar particles thus having half the mass of the original gas particles. Finally, we require an over-density contrast of $\Delta > 55.7$ for the onset of star formation in order to avoid spurious star formation at high redshift.

2.2. Initial conditions

The initial conditions of the Λ CDM model were created assuming scale-invariant adiabatic fluctuations, with the post-recombination power spectrum based on the parametrization of Efstathiou et al. (1992) with a shape parameter of $\Gamma = 0.2$. Throughout this paper we use a WMAP-1 (Spergel et al. 2003) cosmology with a slightly lower Hubble parameter of $h = 0.65^1$ with $\sigma_8 = 0.86$, $f_b = \Omega_b/\Omega_{DM} = 0.2$, $\Omega_0 = 0.3$, and $\Lambda_0 = 0.7$.

The galaxies presented in this paper were simulated at high resolution using the volume renormalization technique (Katz & White 1993; N07) by selecting target halos at $z = 0$ from a low-resolution (128^3 particles) dark matter simulation ($L_{\text{box}} = 50$ Mpc). The target halos

were re-simulated at high resolution by increasing the particle number to 100^3 and 200^3 gas and dark matter particles within a cubic volume at redshift $z = 24$ containing all particles that ended up within the virialized region (conservatively we assumed a fixed radius of 0.5 Mpc) of the halos at $z = 0$. The tidal forces from particles outside the high resolution cube were approximated by increasingly massive dark matter particles in 5 nested layers. The simulated high resolution region was not contaminated by massive particles. A full description of the methods used to generate the initial conditions can be found in Weil et al. (1998).

In N07 we performed simulations of three galaxies at 100^3 and one galaxy at 200^3 resolution in low-density environments. In the present study we expand on this sample by including both lower- and higher-mass galaxies with our final sample covering a mass range of $M_{\text{vir}} = 7 \times 10^{11} - 4 \times 10^{12} M_{\odot}$ at $z = 0$. All galaxies were selected in relatively low-density environments, such that the nearest halo with a mass of $M_{\text{vir}} = 2 \times 10^{11} M_{\odot}$ is more than $1h^{-1}$ Mpc away. Our simulation sample consists of a total of nine simulations, with six models run at 100^3 (Halos L, M, Q, T, U, Y) and three at 200^3 (Halos A2, C2, E2) resolution, see Table 1 for details.

¹ h defined such that $H_0 = 100h \text{ km s}^{-1} \text{ Mpc}^{-1}$.

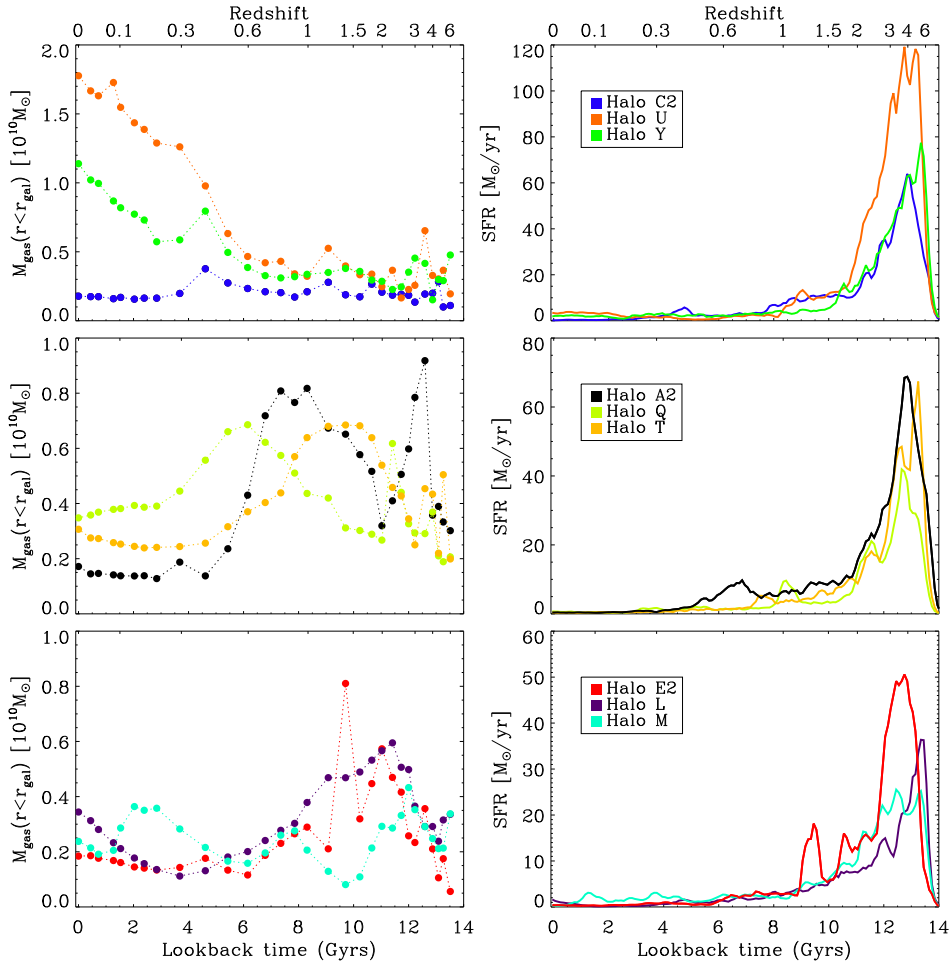


FIG. 2.— The gas masses within the galaxy radii, $r_{\text{gal}} = r_{\text{vir}}/10$ (left panels), together with the star formation histories computed from stellar ages at $z = 0$ (right panels) for the full galaxy sample. For all galaxies the SFR peaks at $z \sim 4 - 5$ after which the rate steeply declines. At low redshifts most galaxies have low gas masses and corresponding very low SFRs, with the exception of galaxies U and Y, which have SFRs of a few solar masses per year caused by late gas inflows.

2.3. Simulation parameters

The gravitational softening length for the 100^3 runs was fixed in comoving units of $\epsilon_{\text{gas}} = \epsilon_{\star} = 0.25$ kpc and $\epsilon_{\text{DM}} = 0.5$ kpc until $z = 9$, and after this the softening remained fixed in physical coordinates at 0.25 kpc for gas and stars and 0.5 kpc for dark matter. The gravitational softening lengths in the 200^3 simulations were set to half compared to the 100^3 simulations, i.e. $\epsilon_{\text{gas}} = \epsilon_{\star} = 0.125$ kpc and $\epsilon_{\text{DM}} = 0.25$ kpc. Thus, our adopted spatial resolution is the same as in N07;J09 and a factor of 2-4 higher than in the studies by Oser et al. (2010, 2012).

Our highest (lowest) resolution runs have particle masses of $m_{\text{stars}} = 1.07 \times 10^5 M_{\odot}$ ($m_{\text{stars}} = 4.5 \times 10^6 M_{\odot}$), $m_{\text{gas}} = 2.14 \times 10^5 M_{\odot}$ ($m_{\text{gas}} = 9 \times 10^6 M_{\odot}$) and $m_{\text{dm}} = 8.6 \times 10^5 M_{\odot}$ ($m_{\text{dm}} = 3.7 \times 10^7 M_{\odot}$) for the stars, gas and dark matter, respectively (see Table 1). The SPH properties of the gas particles were averaged over the usual GADGET-2 spline SPH kernel using $\sim 40 \pm 5$ SPH gas particles and we imposed a minimum hydrodynamical smoothing length equal to $0.1\epsilon_{\text{gas}}$.

We set the parameters governing the multi-phase feedback model as follows: The star formation timescale $t_{\star}^0 = 1.5h^{-1}\text{Gyr}$, $\beta = 0.1$ for a Salpeter IMF (Salpeter

1955), the cloud evaporation parameter $A_0 = 1000$ and the supernova ‘temperature’ $T_{\text{SN}} = 10^8$ K that reflects the heating rate from a population of supernovae for a given IMF. These parameter choices result in a star formation rate (SFR) that is compatible with the observed Kennicutt relation (Kennicutt 1998).

The simulations were run with high force accuracy $\alpha_{\text{force}} = 0.005$ and time integration accuracy $\eta_{\text{acc}} = 0.02$ (see Springel 2005 for details) using the Woodhen machine, a 768 Core Dell Beowulf cluster hosted at the Princeton PICSciE HPC center. The 100^3 resolution simulations required about ~ 5000 CPU hrs on 32 CPUs each, whereas the three 200^3 resolution simulations were expensive with each requiring about $\sim 175,000$ CPU hrs on 64 CPUs.

3. FORMATION HISTORIES OF EARLY-TYPE GALAXIES

3.1. Assembly of the dark matter component

We begin by studying the dark matter (DM) mass accretion histories of our galaxy sample as shown in the left panel of Fig. 1 where we plot the evolution of the virial DM masses as a function of time. The virial radius is defined as the radius enclosing an overdensity of 200 times the critical density ρ_{crit} . Most of the galaxies

assemble their DM component rapidly at high redshifts with typical formation redshifts of the DM component being $z_{f,DM} \sim 1.5 - 1.7$, where $z_{f,DM}$ is defined as the redshift at which half of the final DM component was assembled (see Table 1). Halos U and E2 experience major mergers at $z \sim 1.5$, whereas halos A2, Q, T and L show strong merging activity only at very high redshifts of $z \sim 2 - 3$ followed by relatively quiescent evolution until the present-day, resulting in typical DM formation redshifts of 1.5 for these six galaxies. The remaining halos (C2, Y and M) all experience relatively late major mergers at ($z \sim 1.2$, C2; $z \lesssim 0.5$, Y and M) and thus show lower DM formation redshifts. All galaxies with the exception of halo M have relatively smooth DM accretion histories for the last 5 Gyrs.

Our simulated galaxies were selected in relatively low-density regions, such that the nearest massive halo with $M > 2 \times 10^{11} M_{\odot}$ would be at a distance larger than $1 h^{-1} \text{Mpc}$. In order to quantify the environments of our simulated galaxies more accurately we calculated the mean overdensities of DM in the neighborhood of our target halos. The overdensities were extracted from the original low-resolution simulation by comparing the total DM density in sphere with $r=2 \text{ Mpc}$ centered on the halos with the mean DM density in the simulation box. The resulting Δ_{DM} are listed in Table 1. As expected this quantity is correlated with the final halo mass, with the most massive halos (U and Y) residing in the most overdense regions. However, this correlation is not monotonic, halo Q which is located in the least overdense region does not end up with the lowest final DM mass, as one would naively expect.

In the right panel of Fig. 1 we plot the evolution of the halo spin parameter λ' defined as

$$\lambda' = \frac{J}{\sqrt{2} M_{vir} v_c r_{vir}}, \quad (1)$$

where v_c is the circular velocity at the virial radius r_{vir} and M_{vir} is the virial mass (Bullock et al. 2001). The mergers experienced by halos Y and M at $z \lesssim 0.5$ and halo C2 at $z \sim 1.2$ are clearly identified by sudden jumps in their corresponding spin parameters. At high redshift $z \gtrsim 3$ the evolution of the spin parameter is very spiky for all the halos indicating strong merging activity. The final spin parameter values are consistent with the median value of $\lambda' \sim 0.035$ derived from large numerical simulations (Macciò et al. 2007) with the exception of halos Y and M, which due to their relatively late mergers end up with higher spin values (in the case of halo M significantly higher at $\lambda'_M = 0.1$). In Table 1 we also give the time-averaged spin parameters for all the halos. The effect of mergers increasing the spin parameter (see also Vitvitska et al. 2002) can again be seen for halos Y and M, but interestingly also halos with apparently similar accretion histories such as halos A2 and Q can end up having time-averaged halo spin parameters that almost differ by a factor of three.

3.2. Assembly of the baryonic component

In Fig. 2 we study the baryonic assembly of our galaxies by plotting the total gas mass within the galaxy radii and their star formation rates as a function of time. We define the galaxy radius as $r_{gal} = r_{vir}/10$, meaning that this radius increases with time as the virial radius of the

galaxy grows. In general the gas masses of the galaxies are below $10^{10} M_{\odot}$ during their evolution with typical final gas masses of $\lesssim 3 \times 10^9 M_{\odot}$ (see Table 2). Notable exceptions are the most massive galaxies U and Y, which have significant late gas inflows at $z \lesssim 1$ and end up with final gas masses in excess of $10^{10} M_{\odot}$. The majority of the gas is hot, where hot gas is defined as gas with $T > 2.5 \times 10^5 \text{ K}$ (see Kereš et al. 2005), and thus not directly available for star formation. Interesting exceptions are galaxies Q and M, which both contain significant fractions of relatively cool gas at $z = 0$.

In the right panel of Fig. 2 we show the star formation histories of the galaxy sample computed from stellar ages at $z = 0$. All galaxies start forming their stars in bursts at $z = 4 - 5$ with peak SFRs of $\sim 60 - 120 M_{\odot}/\text{yr}$ for the more massive systems and around $\sim 30 - 50 M_{\odot}/\text{yr}$ for the least massive systems, respectively. Subsequently the SFRs decline almost exponentially, with this decline being faster for the high-mass systems compared to the lower-mass systems. This general trend is only interrupted by occasional mergers that show up as bumps in the star formation histories. At $z = 1$ the typical star formation rates range from $\sim 2 - 10 M_{\odot}/\text{yr}$ and by $z = 0$ they have declined to below $\sim 1 M_{\odot}/\text{yr}$ for all galaxies, but the most massive systems (U and Y), which still exhibit residual star formation rates of a few solar masses per year.

In addition, we calculate the specific star formation rate (SSFR) defined as the $SSFR = SFR/M_*$, where SFR is the total star formation rate and M_* the total stellar mass of the galaxy. The value at $z = 0$ can be found in Table 2, where the current SFR has been calculated using the mean SFR averaged over the last 1 Gyr. Franx et al. (2008); Williams et al. (2009) use the specific star formation rate as an indicator of quiescent red and dead galaxies by defining these galaxies to be systems with $SSFR < 0.3/t_H$, where t_H is the Hubble time at a given redshift. This criterion corresponds to $\log SSFR = -10.7$ at $z = 0$ for our chosen cosmology. Thus, according to this criterion all of our galaxies can be classified as quiescent systems, as they exhibit SSFRs below this threshold value at the present-day (see Table 2). The very low final star formation rates are significant given that the simulations include neither type Ia supernova feedback nor AGN feedback.

3.3. The two phased formation of the stellar component

Following N07 (see also Abadi et al. 2003; Oser et al. 2010; Feldmann et al. 2010) we study the origin of the stellar component in our galaxies by dividing the stellar mass into an in situ component formed within the galaxy ($r < r_{gal}$) and an accreted stellar component formed outside the galaxy ($r > r_{gal}$), where again the galaxy radius is defined as $r_{gal} = r_{vir}/10$ at the corresponding time. The galaxies in our sample are organized into three groups depending on whether their late accretion history ($z \lesssim 2$) is dominated primarily by dissipationless minor merging (mostly accreted stars), a mixed dissipationless/dissipational (mostly accreted and some in situ stars) or a primarily dissipational (significant in situ stars) formation history. We find that this classification of the assembly history divides the simulated galaxies broadly into more massive early-type galaxies with strong size evolution forming dissipationlessly and

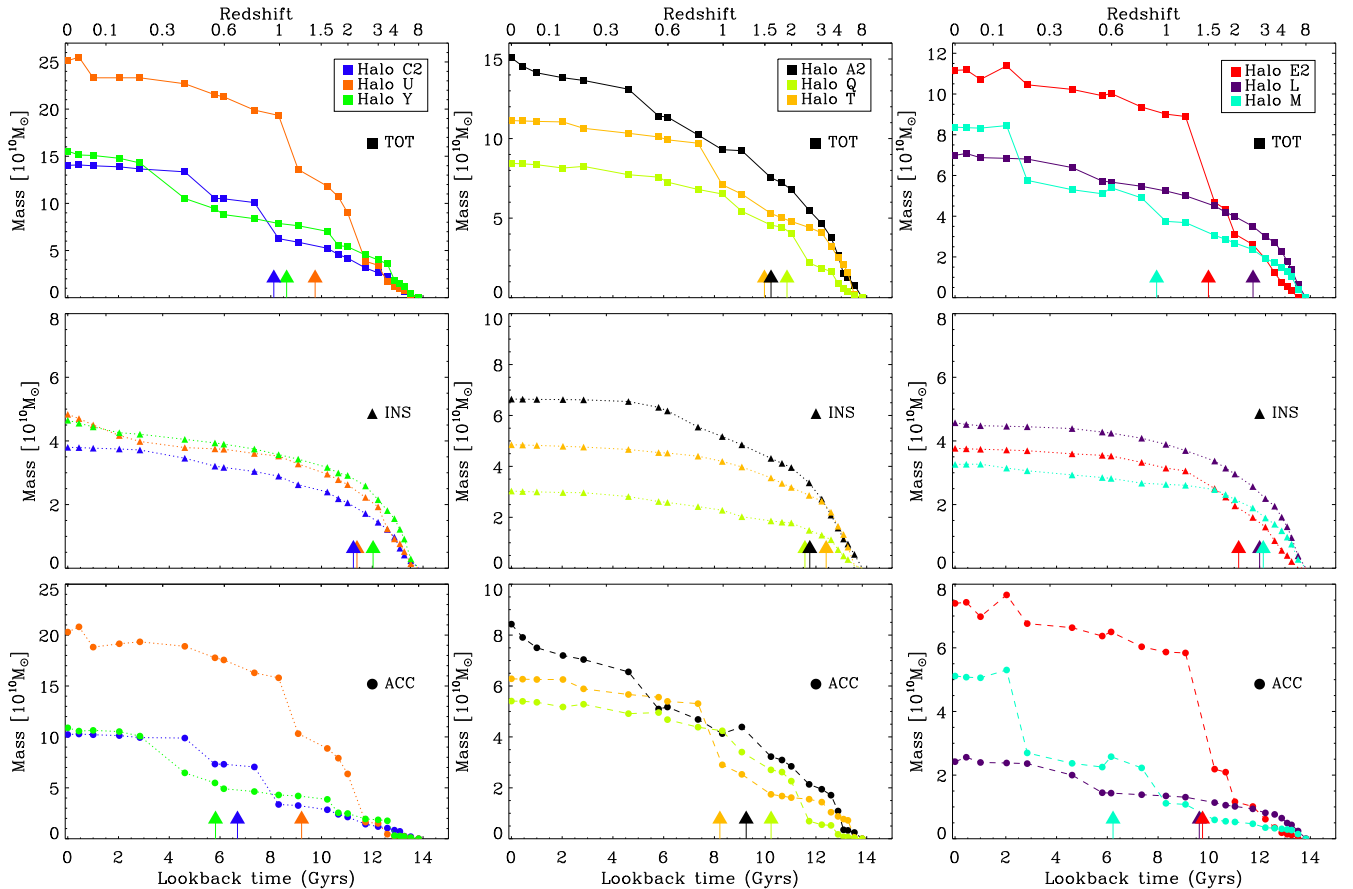


FIG. 3.— The evolution of the total stellar mass (top panels), the in situ formed stellar mass (middle panels) and the accreted (ex situ formed) stellar mass within r_{gal} for our galaxy sample. The arrows indicate the time at which half of the corresponding stellar component was assembled. In all cases the in situ component is formed early, whereas the accreted component is assembled later.

less massive later-type galaxies with weaker size evolution and a more dissipational formation history. The evolution of the accreted and in situ stellar components together with the total stellar mass is shown for our entire galaxy sample in Fig. 3. The galaxies are grouped into three groups of three galaxies depending on whether the majority of the final stellar mass was accreted (C2, U & Y), whether in situ and accreted stellar mass were of roughly equal importance (A2, Q & T) or whether in situ star formation played a dominant role (E2, L & M, see Table 2). Note that although both galaxies M and E2 have more accreted stellar mass at $z = 0$, this is in both cases due to a single major merger and that the stellar masses in both galaxies M and E2 prior to their respective mergers were clearly in situ dominated (see Fig. 4).

The fraction of in situ to accreted stellar mass correlates with galaxy mass, with the more massive galaxies being typically dominated by accreted stars, whereas the least massive galaxies in our sample have significant in situ formed stellar components (see also Oser et al. 2010). However, having said that significant variations exist for galaxies with very similar masses, relatively high-mass galaxies such as galaxy A2 can have significant in situ stellar components and a low-mass galaxy such as galaxy Q can have a significant contribution from accreted stars. Thus, the final total stellar masses alone do not decide the faith of the galaxies rather the details

in the accretion history (i.e. in situ or accretion dominated) are of a significant importance in determining the final properties of the galaxies.

In Fig. 4 we show the absolute contribution of the in situ and accreted stellar components to the total stellar mass at four redshifts. Using this figure and the arrows in Fig. 3 indicating when half of the corresponding stellar component was assembled a clear formation picture emerges. The stellar component in the galaxies forms in a two phased process. At high redshifts ($z \gtrsim 3$) the stellar component in all galaxies is assembled rapidly through in situ star formation, with this star formation being fueled by cold flows (see §4.2) and hierarchical mergers of multiple star-bursting subunits. At later times ($z \lesssim 3$) in situ star formation is a subdominant effect with the majority of the stellar growth proceeding through the accretion of existing stellar clumps.

The galaxies in Fig. 4 are ordered in decreasing final mass from top to bottom. At very high redshifts ($z = 5$) there is no clear correlation between the stellar mass at this redshift and the final stellar mass at $z = 0$. However by $z = 3$ and $z = 1$ at the very latest the most massive galaxies at these redshifts finish as the most massive systems at $z = 0$. Most galaxies have typical formation redshifts of their total stellar components of $z_{f,*} \sim 1.4 - 1.6$ similar to their DM components (see Table 2 and Fig. 3), where $z_{f,*}$ is defined again as the redshift at which half of the final stellar mass was assembled. However, interest-

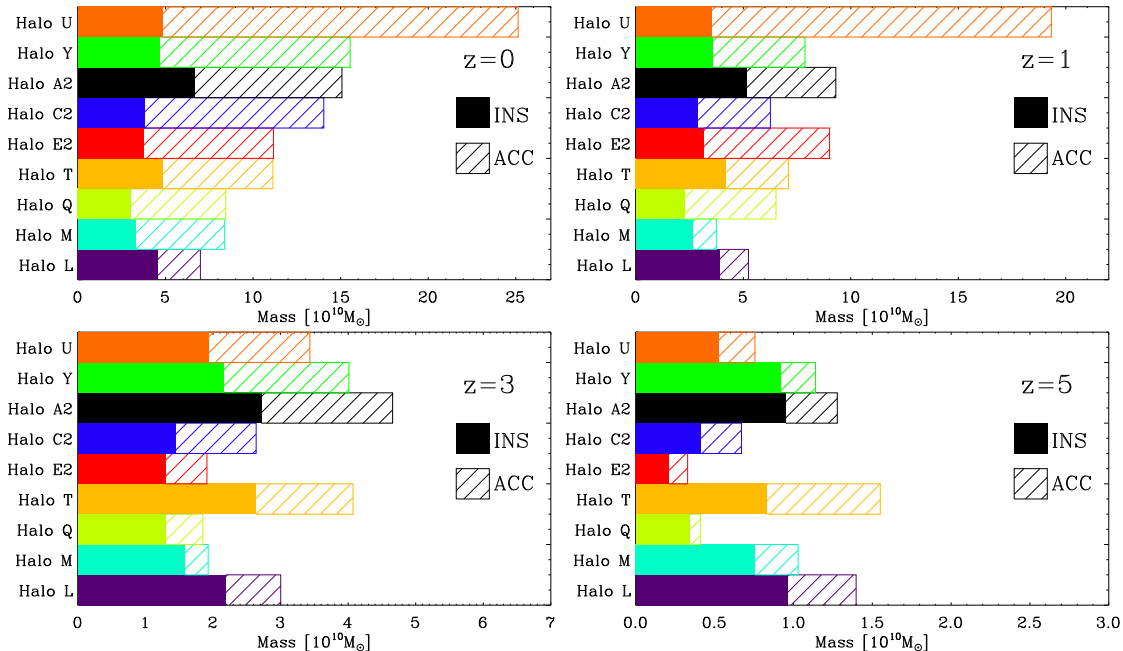


FIG. 4.— The absolute contribution of in situ formed stellar mass (solid colors) and accreted stellar mass (dashed colors) for our galaxy sample shown at $z = 0$ (top left), $z = 1$ (top right), $z = 3$ (bottom left) and $z = 5$ (bottom right). All galaxies assemble rapidly at high redshift through in situ star formation. The late evolution is dominated by accreted stars, with the more massive galaxies ending up with the largest fraction of accreted stars.

ing exceptions exist, galaxies C2, Y and M, which have significant late accretion have $z_{f,*} \sim 1$ and galaxies Q and L, which have very rapid initial growth result in $z_{f,*} \gtrsim 2$. The formation redshifts of the in situ made stars are very similar at $z_{f,ins} \sim 2.5$ for all galaxies, whereas the formation redshift of the accreted stars show a much larger scatter at $z_{f,acc} \sim 0.5 - 1.5$. Again the final stellar mass alone is not the decisive factor, instead there are significant differences in the individual accretion histories for different galaxies in a similar mass range.

Finally we plot the mean ages of the in situ and accreted stellar components as a function of time in Fig. 5, where the stellar ages are always normalized to the age of the Universe at the corresponding redshift. Studying this figure a clear systematic trend can be discerned. The mean age of the accreted stellar component is always older than the in situ formed stars. This can be understood naturally in a hierarchical Universe as the majority of the accreted stars form individually in low-mass systems at high redshifts, whereas in situ star formation proceeds at a slower rate in the more massive systems. Thus, the accreted stars are typically formed earlier and are older compared to the in situ component. Furthermore, as discussed above the most massive galaxies typically have a higher fraction of accreted stars and hence have older mean stellar ages. The notion of a two phased galaxy formation process thus naturally explains the counter-intuitive concept of downsizing. Massive galaxies form their stellar core mass in situ and then accrete substantial amounts of stars that were formed even earlier in smaller subsystems. Hence by $z \sim 2-3$ the most massive galaxies have the oldest stellar populations compared to lower mass galaxies that have still significant in situ star formation and much lower contribution from accreted stars. This trend is in good agreement with

observations (e.g. Glazebrook et al. 2004; Juneau et al. 2005; Bundy et al. 2006; Cimatti et al. 2006) and theoretical models (e.g. Guo & White 2008; Shankar et al. 2011; Yang et al. 2011), and a natural outcome of the two phased galaxy formation process. At the present-day the mean stellar ages are typically high at $age_* \gtrsim 11.2$ Gyr for all our galaxies, except galaxy M, which due to its very late merger has a somewhat younger stellar population at $age_* \sim 10.6$ Gyr (see Table 2).

3.4. Size evolution of early-type galaxies

We then turn our attention to the size growth of our simulated early-type galaxies by studying the evolution of their projected half-mass radii in Fig. 6, where we plot separately the evolution of $R_{1/2}$ for the total stellar component (top panel), the in situ formed component (middle panel) and the accreted stars (bottom panel). All galaxies grow in size by increasing their half-mass radii by factors of several between $z = 3$ and the present-day. However, studying Fig. 6 it is clear that the in situ and accreted stellar components grow very differently. For most galaxies the size growth of the in situ component is very modest with $R_{1/2,ins}$ growing from ~ 0.5 kpc at $z \sim 2$ to ~ 1.5 kpc at $z \sim 0$. The in situ stars thus form typically at similar small radii in the bulge components of all the galaxies, regardless of the galaxy mass. The situation for the accreted stellar component is very different with strong evolution in $R_{1/2,acc}$ from $\lesssim 1$ kpc at $z \sim 2$ to $\gtrsim 3$ kpc at the present-day.

In the two phased formation mechanism the inner parts of the galaxies are built up primarily from in situ formed stars, whereas the other parts contain predominantly accreted stars, which are thus responsible for the observed size growth of early-type galaxies (e.g. Trujillo et al. 2006, 2007; van Dokkum et al. 2008, 2010). The accreted

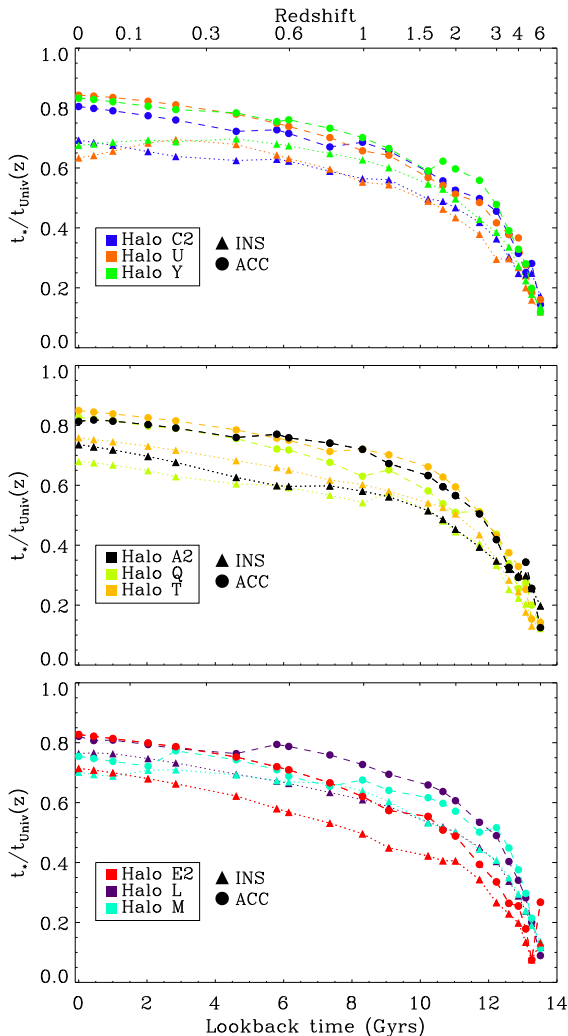


FIG. 5.— The evolution of the mean age of the in situ formed (triangles) and accreted stars (circles). The stellar ages are normalized to the age of the Universe at the corresponding redshift. In all cases the mean age of the accreted stellar component is older than the age of the younger in situ formed component.

stars are added to the galaxies primarily through dry minor mergers, which are very efficient in increasing the final size of the system and decreasing the final central density as demonstrated in Naab et al. (2009), see also Bezanson et al. (2009). Thus, we expect the amount of size growth to correlate with the stellar accretion histories, with the systems having the largest amount of accreted stars also showing the strongest size growth. Indeed, this is seen with the sample with a dominant component of accreted stars (C2, U & Y) showing average growth in size between $z \sim 3$ and $z \sim 0$ by a factor of ~ 7.9 , for the samples with galaxies (A2, Q & T) and (E2, L & M) the average growth factors are ~ 6.6 and ~ 5.9 , respectively. In the case of galaxy M we also see that a late major merger is not that efficient in increasing the size of the galaxy, with the final $R_{1/2}$ being only marginally larger than the pre-merger half-mass radius (see also Naab et al. 2009). Finally, as the typical stellar accretion history is mass dependent favoring more accreted stars over in situ stars for increasing galaxy mass, we expect that the size evolution will be mass depen-

dent with the most massive galaxies experiencing the strongest size growth. This finding is also in agreement with the results found by (Oser et al. 2010, 2012) who used a larger galaxy sample simulated at somewhat lower resolution. Finally we note that the resulting size growth as a function of redshift is much stronger when compared to the corresponding plot in N07 (their Fig. 9). The reason for this is a different definition of the accretion radius. In the present study we calculate the half-mass radii of the in situ and accreted component within the galaxy radius ($r_{\text{gal}} = r_{\text{vir}}/10$), whereas in the N07 study we used a fixed physical radius of 30 kpc for all redshifts. The definition used in N07 overestimates the half-mass radii of the accreted component at high redshifts and results in a much smaller size growth compared to the definition used in this paper.

Related to the size growth we plot in Fig. 7 the circular velocity profiles, defined as $v_c^2 = GM(r)/r$ for our galaxy sample at redshifts of $z = 0$ (top panel), $z = 1$ (middle panel) and $z = 3$ (bottom panel). We also give in this plot the corresponding projected half-mass radii of the total stellar component, demonstrating explicitly the size growth of the galaxies from $z = 3$ to the present-day. At high redshifts the galaxies are compact with their rotation curves peaking at relatively high values of $v_c \sim 450$ km/s, however none of our galaxies show extreme rotation curves with peaks in excess of $v_c \gtrsim 750$ km/s as found by Meza et al. (2003) and Joung et al. (2009). With increasingly lower redshifts the peaks of the rotation curves are systematically shifted to larger radii and also lowered in absolute value demonstrating the size growth of the parent galaxies. At the present-day the peak of the rotation curve is typically in the range of $v_c \sim 300 - 400$ km/s with only the most massive system (galaxy U) having a rotation curve peaking at $v_c \sim 450$ km/s (see Table 1). All of our systems are also clearly baryon dominated in their inner regions with the DM fraction being typically low at $f_{\text{DM}} \sim 0.1 - 0.3$ within the central 3D half-mass radii (see Table 2).

Comparing our rotation curves to the ones presented in N07 for simulations without supernova feedback we see that the rotation curves in the present study peak at values higher by roughly ~ 100 km/s. In addition, the rotation curves with supernova feedback are also somewhat more centrally peaked indicating a more massive central bulge component. The main reason for this difference lies in the different star formation threshold. The density threshold quoted in the N07 paper $\rho_{\text{th}} = 7 \times 10^{-26} \text{ g cm}^{-3}$ was missing a factor of $h^2 = 0.65^2$ and thus the density threshold actually used in the N07 paper was $\rho_{\text{th}} = 7 \times 10^{-26} h^2 \text{ g cm}^{-3}$ corresponding to $n_{\text{th}} = 0.019 \text{ cm}^{-3}$, which is about a factor of ten lower than in the present study. In the no feedback simulations presented in N07 stars were very efficiently formed already in infalling subclumps. In the current simulations star formation is somewhat delayed due to the higher star formation threshold and the inclusion of supernova feedback. Thus the gas is required to reach higher densities in the central regions of the galaxy before it can be turned into stars, thus explaining the slightly higher and more peaky rotation curves of our current simulation sample. However, given the relatively weak supernova feedback employed in the present study, the main reason for the higher values of the central rotation curves

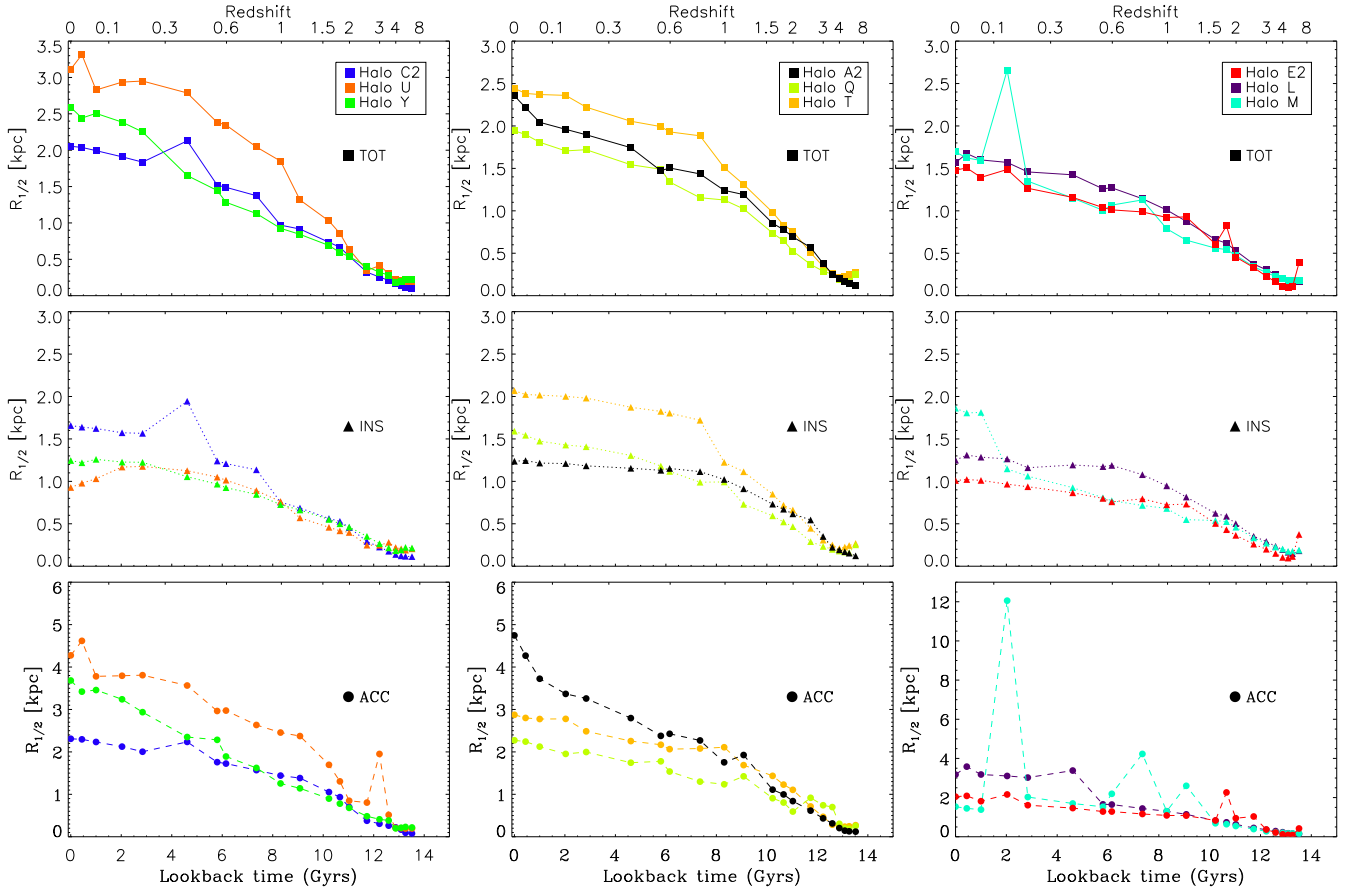


FIG. 6.— The evolution of the projected half mass radius for all stars (top panels), for the in situ formed stars (middle panel) and for the accreted stars (bottom panel) for our galaxy sample. The evolution of the projected half mass radius remains relatively flat for the in situ component. On the contrary the half mass radius of the accreted component evolves strongly resulting in a size evolution of the total stellar component.

in this study compared to N07 remains the difference in the employed density threshold for star formation. Outside the central ($r \lesssim 3$ kpc) bulge-dominated region all rotation curves are relatively flat showing a constant rotation curve in relatively good agreement with observations (e.g. Bolton et al. 2008; Coccato et al. 2009; Napolitano et al. 2009, 2011). Finally, we reproduce a key finding of N07 who showed that increasing numerical resolution lowers the peak of the rotation curve and makes it overall flatter. In the top right panel of Fig. 7 we plot as an comparison the rotation curve of galaxy E run at 100^3 resolution (E1) and compare it our standard simulation of the same initial conditions at 200^3 resolution (E2). Increasing the resolution from 100^3 to 200^3 lowers the peak of the rotation curve by ~ 40 km/s and makes the overall shape somewhat flatter in good agreement with the findings presented in N07.

3.5. Evolution of the dark matter fractions

In Fig. 8 we study the evolution of the dark matter properties of our simulated galaxies by showing the dark matter fractions inside the three-dimensional half-mass radius (r_{3D}) as a function of redshift. At high redshifts the simulated galaxies are all very strongly baryon dominated due to gas feeding in cold gas flows and the ensuing rapid in situ star formation. Typical dark matter fractions within one r_{3D} at $z \sim 4 - 5$ are very low at

$f_{DM} \lesssim 0.05$. At lower redshifts of $z \lesssim 3$ the importance of in situ star formation is reduced and the majority of the stellar growth proceeds through stellar dry accretion. For most galaxies the final dark matter fractions are established at $z \sim 1.5 - 2$ after which they remain more or less constant. The exceptions being galaxies U and Y, which both have significant late gas inflows (see §3.2) that also drag in DM increasing the overall dark matter fractions below $z \lesssim 1$. The final dark matter fractions at the present-day for our galaxy sample within one r_{3D} are in the range of $f_{DM} \sim 0.1 - 0.3$ (see Table 2).

Our simulated dark matter fractions can be compared to recent observations that in a self-consistent way combine the constraints from both gravitational lensing and stellar kinematics and derive estimates of the dark matter fractions of early-type galaxies (e.g. Koopmans et al. 2006; Auger et al. 2009, 2010; Barnabè et al. 2009, 2011). The derived dark matter fractions from these observational studies are sensitive to the stellar initial mass function (IMF) with a Chabrier IMF typically resulting in dark matter fractions that are larger roughly by a factor of two compared to the dark matter fractions derived using a Salpeter IMF (see e.g. Auger et al. 2010). The observed dark matter fractions derived using a Salpeter IMF seem to cluster in the range $f_{DM} \sim 0.1 - 0.3$ in good agreement with our simulated results (Koopmans et al. 2006; Auger et al. 2009 and see also Grillo & Gobat

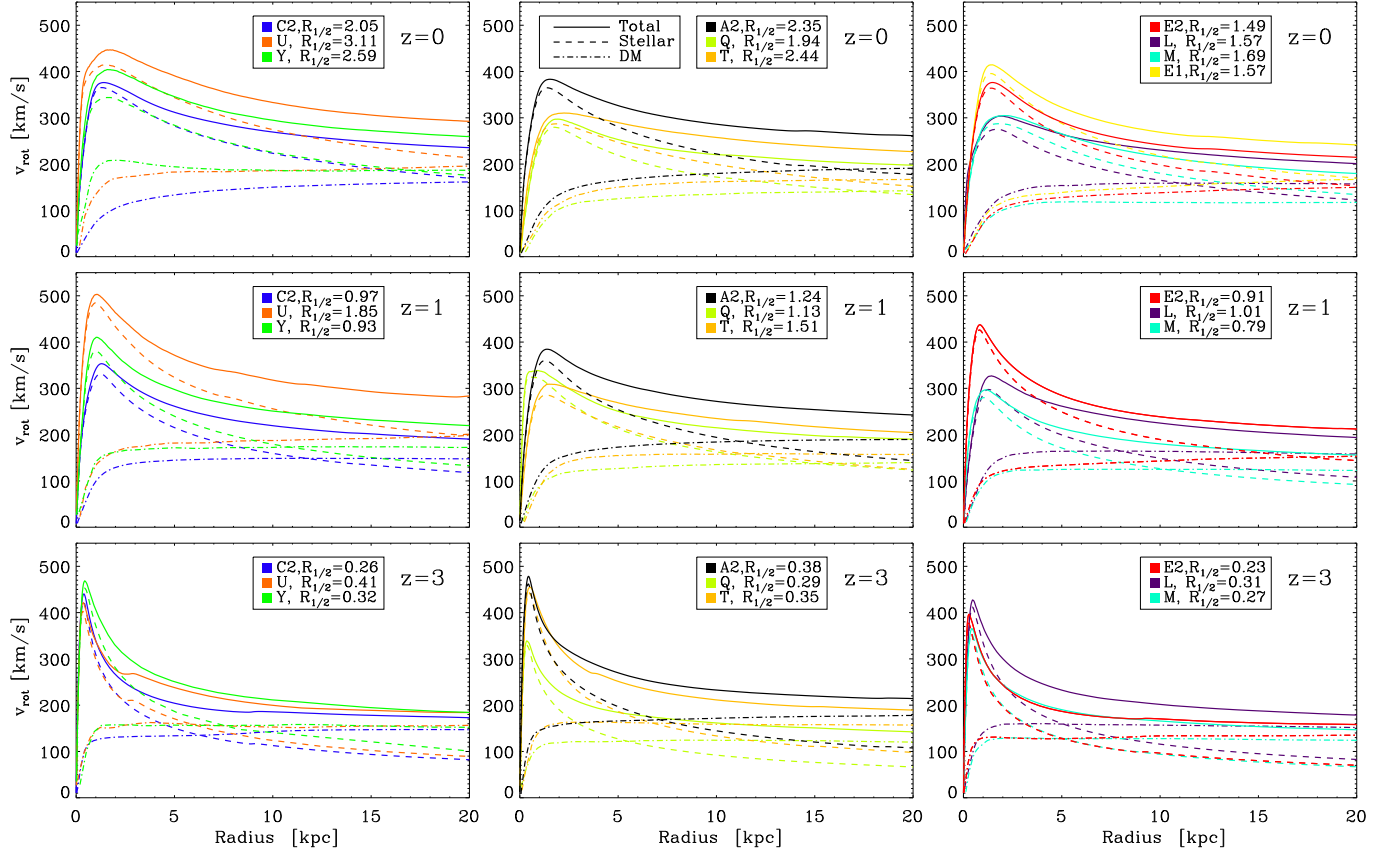


FIG. 7.— The circular rotation curves for our galaxy sample at $z = 0$ (top panel), at $z = 1$ (middle panel) and at $z = 3$ (bottom panel). In addition the projected half mass radii at the corresponding redshift is given. In order to demonstrate the importance of numerical resolution we plot in the top right panel the rotation curves for halo E at both 200^3 (E2) and 100^3 (E1) resolution. All galaxies are dominated by luminous matter in their central parts within a few half-mass radii.

2010; Grillo 2010; Leier et al. 2011). Given our limited statistics we also see hints of a weak trend with mass, with the more massive galaxies having on average slightly larger dark matter fractions of $f_{\text{DM}} \sim 0.2$ with the lower mass galaxies clustering around a value of $f_{\text{DM}} \sim 0.1$. The general trend of larger dark matter fractions for more massive galaxies is in broad agreement with the observational data (e.g. Auger et al. 2010).

Following Koopmans et al. (2006) we fit the total density profile of our simulated galaxies using the profile

$$\rho_{\text{tot}}(r) = \rho_0 \left(\frac{r}{r_0} \right)^{-\gamma'}, \quad (2)$$

where ρ_0 can be uniquely determined and r_0 can be set arbitrarily (we chose $r_0 = r_{3D}$). The only remaining free parameter in the density distribution is then the logarithmic density slope $\gamma' = -d \log \rho_{\text{tot}} / d \log r$, which we fitted between 0.1 kpc and $3r_{3D}$. The fitting procedure is insensitive to a cutoff beyond several half-mass radii, but significantly more sensitive to the cutoff at the inner radius. Tests showed that the chosen cutoff radii provided a robust and fair estimate of the central total density profiles for our simulated galaxies. In Fig. 9 we show the evolution of the logarithmic density slope γ' as a function of time for our simulated galaxies. At high redshifts all of the galaxies are baryon dominated and the corresponding density profile is very steep with $\gamma' \sim 3$. At

lower redshift the fractions of dark matter within the half mass radii increases and the corresponding total density profiles become flatter, with all galaxies approaching the isothermal value of $\gamma' \sim 2$ by the present-day. The mean density slope of all our galaxies at $z = 0$ is $\langle \gamma' \rangle = 2.06$ with an intrinsic scatter of $\Delta \sim 0.2$. This is in excellent agreement with the latest observational determinations, which found $\langle \gamma' \rangle = 2.078 \pm 0.027$ for a sample of 73 early-type galaxies (Auger et al. 2010). Again, given our rather limited sample we cannot draw strong conclusions concerning the mass dependence of γ' . However, we find that the more massive galaxies typically have larger values of $\gamma' \sim 2.2$ at $z = 0$, whereas the lower mass galaxies typically show γ' values below the isothermal limit of $\gamma' \sim 1.9$. Again, the trend of more massive galaxies typically having larger values of γ' is in agreement with recent observations (e.g. Auger et al. 2010).

Finally, we perform the fit of Eq. (2) to the dark matter profiles of our galaxies in Fig. 10, where $\gamma'_{\text{DM}} = -d \log \rho_{\text{DM}} / d \log r$ is the logarithmic density profile of the dark matter only without the baryonic component. The fits were now performed between 0.25 kpc and $3r_{3D}$ due to the larger softening length of the dark matter component. Typically γ'_{DM} peaks at a value of $\gamma'_{\text{DM}} \sim 1.5 - 2$ at redshifts of $z \sim 2 - 3$, after which the slope flattens reaching values of $\gamma'_{\text{DM}} \sim 1.2 - 1.5$ by the present-day. This evolution is particularly well seen in the high reso-

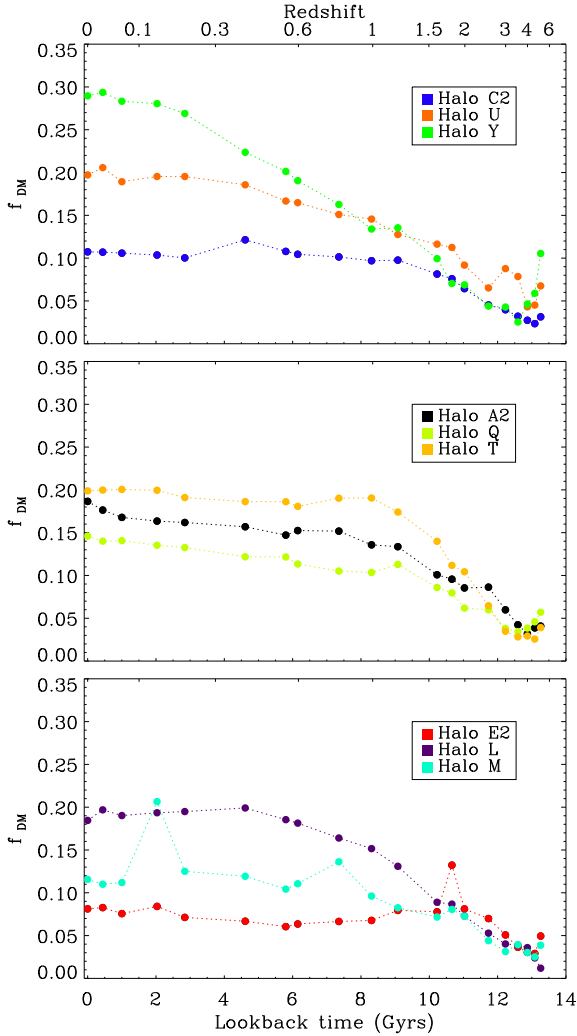


FIG. 8.— The evolution of the dark matter fraction inside the three dimensional half mass radius as a function of redshift for our simulated galaxy sample. At high redshifts the dark matter fractions are typically very low at $f_{DM} \sim 0.05$, with the fractions increasing by a factor of a few to $f_{DM} \sim 0.1 - 0.3$ by the present-day.

lution simulations A2, C2 and E2, which have very well determined dark matter slopes also at the highest redshifts. The exceptions to this trend are again galaxies U and Y, which both have late inflows of gas and dark matter resulting in steepening dark matter profiles at low redshifts. The initial adiabatic contraction of the dark matter profiles followed by a gradual flattening of the profiles at lower redshifts is broadly consistent with expectations from gravitational feedback heating (see §4.4).

3.6. Evolution of the baryon conversion factor

We end this Section by studying the galaxy formation efficiency. In order to do this we define the baryonic conversion parameter f_{conv} as

$$f_{conv} = \frac{m_{*,gal}}{m_{DM,vir}} \bigg/ \frac{\Omega_b}{\Omega_{DM}} = \frac{m_{*,gal}}{f_b \times m_{DM,vir}}, \quad (3)$$

where $f_b = \Omega_b/\Omega_{DM} = 0.2$ is the baryon fraction, $m_{*,gal}$ is the total stellar mass in the central galaxy and $m_{DM,vir}$ is the total DM mass within the virial radius. In effect

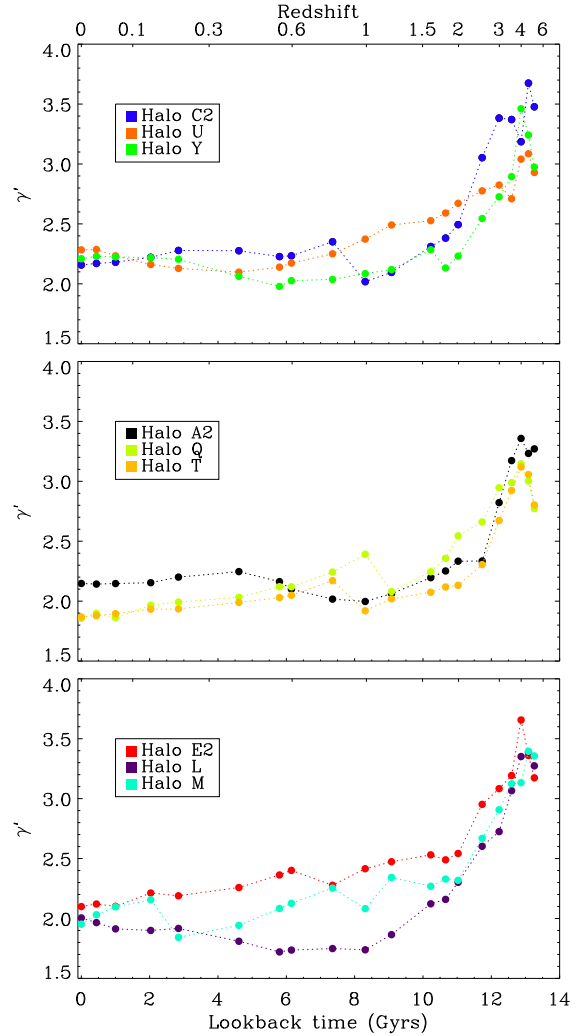


FIG. 9.— The evolution of the total logarithmic density slope $\gamma' = -d \log \rho_{tot} / d \log r$ as a function of redshift for our simulated galaxy sample. At high redshifts the galaxies are baryon dominated and the total density profiles are typically steep at $\gamma' \sim 3$. At lower redshifts the dark matter fractions in the galaxies increase and the density slopes flatten towards values of $\gamma' \sim 2$ at $z = 0$.

the conversion factor, f_{conv} , thus tells us what fraction of the total available baryonic mass in the halo is locked in the central stellar component. In Fig. 11 we show the evolution of the conversion factor as a function of time. At high redshifts ($z \gtrsim 2$) the evolution of the galaxies is driven by multiple mergers resulting in a spiky evolution of the conversion factor reaching very high values of $f_{conv} \sim 0.8$. The subsequent evolution is quieter with f_{conv} remaining more or less constant below $z \lesssim 1$, with the exception being galaxy M, for which the late merger shows up as a marked increase in the conversion factor.

At the present-day our galaxies have typical conversion factors of $f_{conv} \sim 0.4 - 0.6$ (see Table 2). These values are about a factor of $\sim 2 - 3$ higher than the values predicted from halo occupation statistics, in which dark matter halo masses are matched to central stellar masses assuming a one-to-one monotonic relationship (Guo et al. 2010; Moster et al. 2010). These studies find that the galaxy formation efficiency peaks with a conversion factor of $f_{conv} \sim 0.2$ for halo masses of

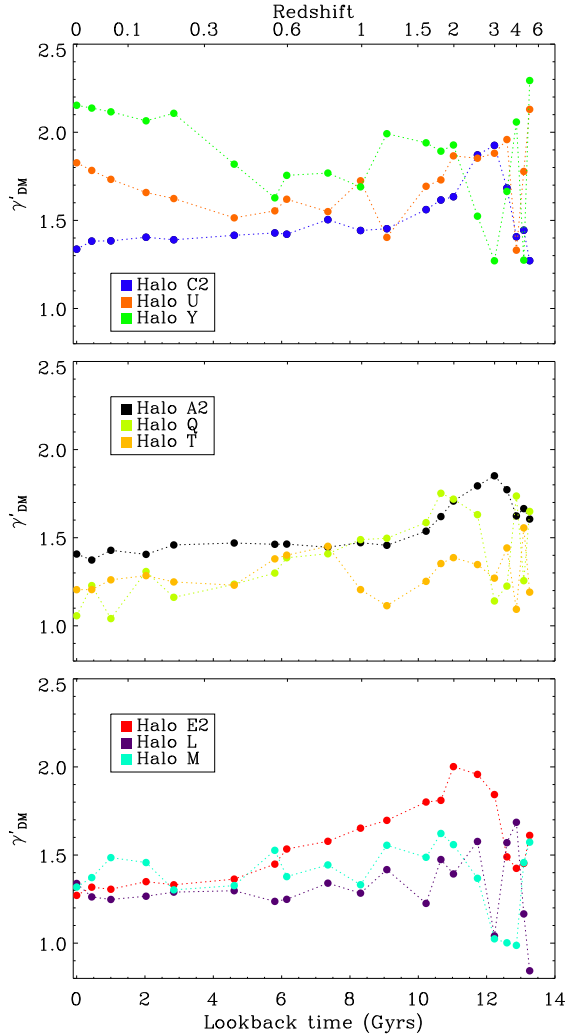


FIG. 10.— The evolution of the logarithmic dark matter density slope $\gamma'_{\text{DM}} = -d \log \rho_{\text{DM}} / d \log r$ as a function of redshift for our simulated galaxy sample. The dark matter slopes typically peak at $z \sim 2 - 3$ after which they gradually flatten until $z = 0$.

$M_{\text{halo}} \sim 6 \times 10^{11} M_{\odot}$. Our simulated halo masses at $z = 0$ are $M_{\text{halo}} \sim 8 \times 10^{11} - 4 \times 10^{12} M_{\odot}$ and should thus contain galaxies with conversion factors of $f_{\text{conv}} \sim 0.2$, which is clearly not the case. Furthermore weak lensing studies by Mandelbaum et al. (2006) indicate that galaxies with central stellar masses of $M_{*,\text{cen}} \sim 11.2 \times 10^{10} M_{\odot}$ (typical stellar masses for our galaxy sample, see Table 2) should have corresponding DM halos with masses of $M_{\text{DM,vir}} \sim 34_{-9}^{+10} \times 10^{11} h^{-1} M_{\odot}$, which would result in conversion factors of $f_{\text{conv}} \sim 0.16_{-0.05}^{+0.10}$.

The conversion factor declines rapidly both towards lower and higher masses around the peak halo mass of $M_{\text{halo}} \sim 6 \times 10^{11} M_{\odot}$ (Guo et al. 2010). Towards lower masses this decline is most probably caused by UV and X-ray heating and supernova driven winds, which are able to expel significant amounts of gas from dwarf galaxies (e.g. Oppenheimer & Davé 2006; Hambrick et al. 2011a), whereas for systems more massive than the peak halo mass the reduction in f_{conv} is possibly due to an increasing contribution from feedback from supermassive BHs at the centers of the galaxies, which is able to expel

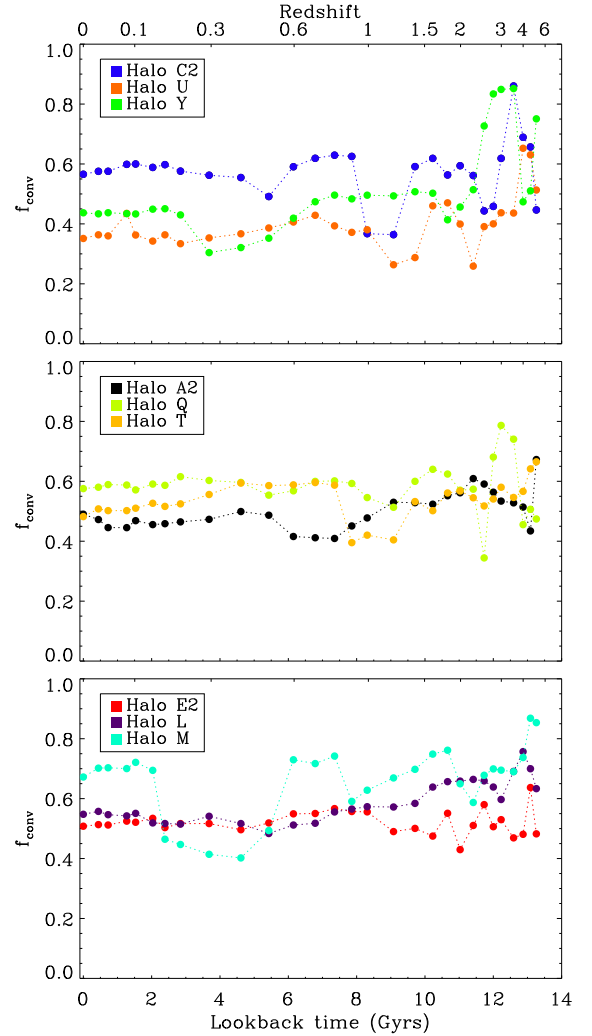


FIG. 11.— The evolution of the baryon conversion efficiency, i.e. the fraction of available baryonic mass locked in stars in the central galaxy. Typical values of $f_{\text{conv}} \sim 0.4 - 0.6$ are a factor of 2-3 higher than expected from halo occupation statistics.

gas (e.g. McCarthy et al. 2010).

These effects are not included in the present study, thus it is not too surprising that our simulated conversion factors are too high by a factor of 2-3. The main question is how the inclusion of these effects would influence the relative contribution of in situ formed and accreted stars to the final stellar component. Supernova driven winds are most efficient in suppressing star formation in small systems and hence would primarily affect the accreted stellar component that is formed on average in smaller galaxies (Governato et al. 2010; Agertz et al. 2011; Guedes et al. 2011). However, also more massive systems are influenced by supernova driven winds and thus also the formation of the in situ component would be slowed down. AGN feedback is only important in massive galaxies and would thus preferentially inhibit late in situ star formation in the most massive galaxies (Teyssier et al. 2011; Debuhr et al. 2011; Dubois et al. 2012). Thus, although the inclusion of both these effects would certainly lower the overall total stellar masses, the relative contribution of in situ and accreted stellar mass might not be significantly affected. The effect of dif-

ferent feedback prescriptions on the resulting conversion factor is an interesting issue that deserves further study, but is outside the scope of the present study (see also Piontek & Steinmetz 2011).

4. EVOLUTION OF THE GAS COMPONENT IN EARLY-TYPE GALAXIES

4.1. Temperature structure of the gas

In this Section we discuss the evolution of the gaseous component of early-type galaxies by using the evolution of halos C2, U, A2 and E2 as representative examples. We begin by summarizing the evolution of the gas temperatures in Fig. 12 for the galaxies at redshifts of $z = 0, 1, 3, 5$ by showing the temperature profiles (left panel), the entropy distributions (middle panel) and the phase-space diagrams (right panel) for all gas within the virial radius. The temperature of the gas is increasing with decreasing redshift from typical values of $T \sim 10^5$ K at $z = 5$ to temperatures above $T \sim 10^6$ K at $z = 0$. There is also a clear trend with halo mass, with more massive galaxies (halo U) showing higher gas temperatures indicating that the halo gas is maintained at thermal virial equilibrium. Towards the center a drop in temperature can be seen indicating cooling gas, however in the very central parts of the galaxies the temperature is rising again due to the input from supernova feedback energy in starforming particles.

In the middle panel of Fig. 12 we plot the distribution of the gas entropy, defined as $S = kTn^{-2/3}$ for the four galaxies. The cooling time is defined as

$$t_{\text{cool}} = \left(\frac{S}{10 \text{ keVcm}^2} \right)^{3/2} \frac{1.5(\mu_e/\mu)^2 \cdot (10 \text{ keVcm}^2)^{3/2}}{(kT)^{1/2}\Lambda(T, Z)}, \quad (4)$$

where k is the Boltzmann constant, $\Lambda(T, Z)$ is the cooling function, and $\mu \simeq 0.59$, $\mu_e \simeq 1.1$ are the mean molecular weight and mean molecular weight per electron, with the values given for a fully ionized gas. The first term in the equation is a measure of the entropy and therefore an adiabatic invariant, whereas the second term only depends on the temperature (T) and metallicity (Z) of the gas through the cooling function (Scannapieco & Oh 2004; Khalatyan et al. 2008). The second factor in Eq. 4 has an absolute minimum, corresponding to $t_{\text{cool}} \sim 2$ Gyr for our primordial cooling function. In Fig. 12 we also plot the entropy values corresponding to minimum cooling times of 0.1, 1 and 10 Gyr as dashed lines as well as the entropy of neutral gas at $T \sim 10^4$ K marked with $S_{\text{max,SF}}$. Gas with entropy below this limit is rapidly cooling and destined to form stars. At high redshifts the entropy distribution of the gas is bimodal with cold, high-density, star-forming gas forming a low entropy peak and lower density, hot shock-heated gas forming a high entropy peak. At lower redshifts the majority of the low entropy gas has been consumed by star formation, however in contrast to the no feedback simulations studies in J09 some low entropy gas capable of star formation remain at intermediate redshifts of $z \sim 1$. Having said that, the majority of gas ($\gtrsim 90\%$) by $z \sim 1$ and virtually all of the remaining gas by $z \sim 0$ is dilute shock-heated gas with correspondingly long cooling times of the order of $t_{\text{cool}} \sim 5 - 10$ Gyr.

In the right panel we show the phase-space diagrams for our galaxies, where the density is given as the density

over the mean baryonic density at the corresponding redshift. Also here the bimodality of the gas distribution can be seen with gas divided into a low-density hot component and a higher density star-forming cold component. The fraction of hot gas (defined as $T > 2.5 \times 10^5$ K and $\rho < \rho_{\text{th}}$) is increasing steadily with decreasing redshift from $f_{\text{hot}} \lesssim 20\%$ at $z = 5$ to $f_{\text{hot}} \lesssim 50\%$ at $z = 3$. Starforming gas with densities above the star formation threshold ρ_{th} is clearly visible in the plot as most of the particles can be found on an equilibrium curve in the $\rho - T$ plane dictated by the self-regulated feedback model (Springel & Hernquist 2003). In this subresolution model feedback from supernovae adds thermal energy to the ISM, pressurizing the equation-of-state (EOS) and making it stiffer with respect to an isothermal EOS. The effective EOS can be written as

$$P_{\text{eff}} = (\gamma - 1)\rho u_{\text{eff}} \quad (5)$$

where γ , ρ and u_{eff} are the ratio of specific heats, total gas density and effective specific thermal energy, respectively. The effective energy is the weighted average of a cold gas component kept fixed at $T \sim 1000$ K at a typical mass fraction of $x \sim 0.9$ and a hot supernova heated gas component at $T \sim 10^8$ K with a typical mass fraction of $x \sim 0.1$ (see Springel & Hernquist 2003 for further details). Following Robertson et al. 2004 we fit the EOS with a third order polynomial that is accurate within 1% for densities above the star formation density threshold of $n_{\text{th}} > 0.205 \text{ cm}^{-3}$ or $\log n_{\text{th}} > -0.69$,

$$\log P_{\text{eff}} = 0.031 (\log n_{\text{H}})^3 - 0.228 (\log n_{\text{H}})^2 + 1.902 \log n_{\text{H}} - 11.5, \quad (6)$$

where the pressure and number density are given in cgs-units, $[P_{\text{eff}}] = \text{erg cm}^{-3}$ and $[n_{\text{H}}] = \text{cm}^{-3}$, respectively. Differences in the numerical factors with respect to Robertson et al. (2004) are due to the fact that we use slightly different values for the cooling rates of a primordial gas adopted from Theuns et al. (1998), which result in a somewhat different threshold density and corresponding fit to the stiffened EOS. A few gas particles can be seen lying above this equilibrium curve. These are particles that have just received a significant energy injection from supernova feedback and are now cooling onto the equilibrium curve on the temperature decay scale set by the self-regulated feedback parameters (see Eq. 12 of Springel & Hernquist 2003).

Finally, we can derive estimates of the amount of cold molecular gas in our galaxies indirectly by using the crude approximation that about $\sim 90\%$ of the star-forming gas above the density threshold of $n_{\text{th}} > 0.205 \text{ cm}^{-3}$ is in a very cold phase ($T \sim 1000$ K) with the remaining $\sim 10\%$ being supernova heated gas as dictated by our equilibrium supernova feedback model (Springel & Hernquist 2003). At high redshifts the gas dynamics is driven by cold gas flows and the corresponding star formation fractions are very high at $f_{\text{SF}} \sim 50 - 60\%$ (see §4.3). As a result the predicted masses of cold molecular gas at $z = 5$ are of the order of a few times $10^9 M_{\odot}$. At the present-day the starforming gas fractions for all of our simulated galaxies are below $\lesssim 1\%$ and as result the expected cold molecular masses at $z = 0$ are of the order a few times $10^7 M_{\odot}$ in good agreement with recent observations of the typical molecular masses of

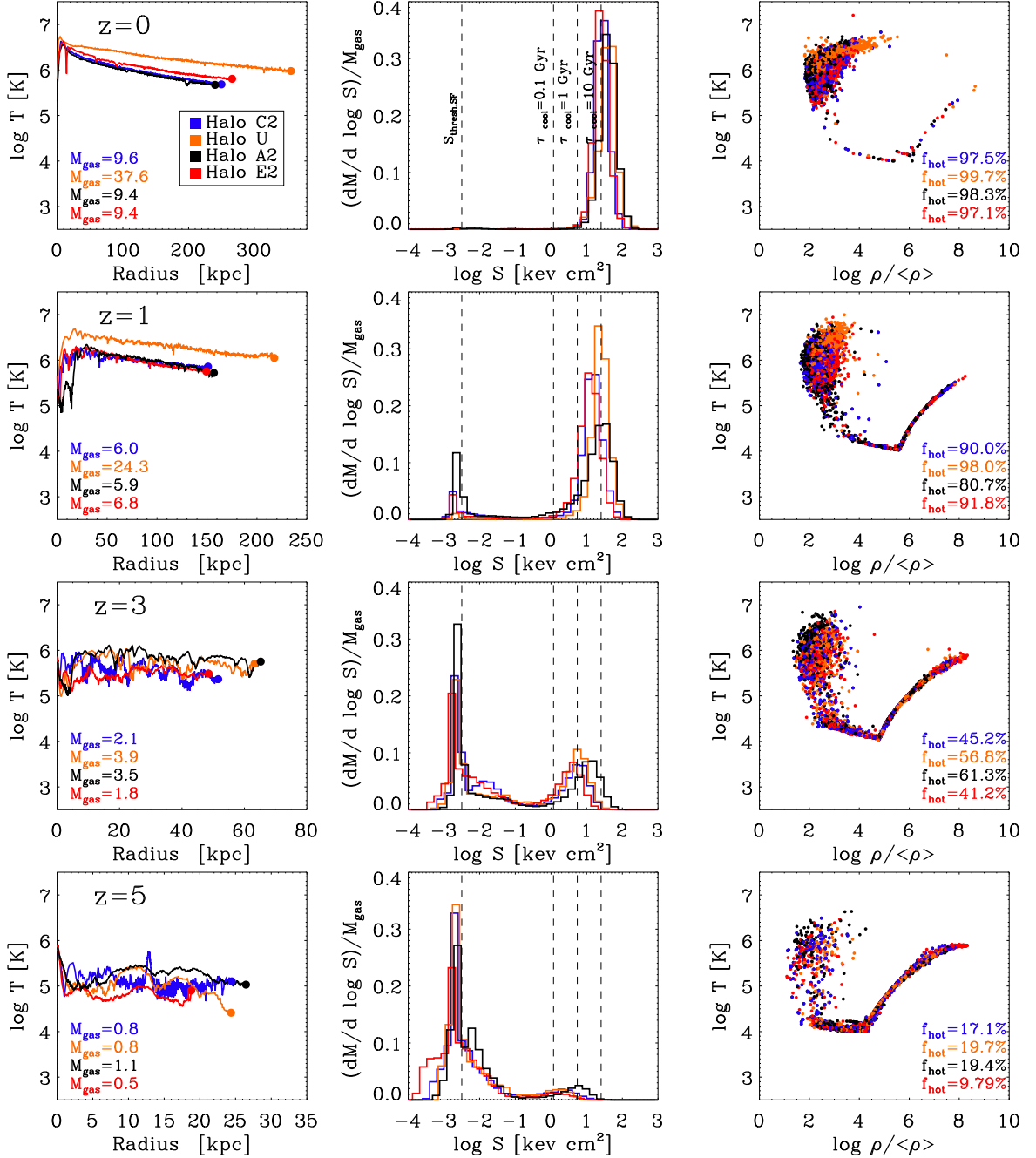


FIG. 12.— Evolution of the temperature profile (left panel), the entropy distribution (middle panel) and the phase-space diagram (right panel) of all gas within r_{vir} as a function of redshift (top to bottom) for halos C2 (blue), U (orange), A2 (black), and halo E2 (red), where M_{gas} is the virial gas mass in units of $10^{10} M_{\odot}$ and f_{hot} is the fraction of diffuse gas with $T > 2.5 \times 10^5$ K and $\rho < \rho_{\text{th}}$. The temperature of the diffuse gas is steadily increasing with decreasing redshift and the entropy distribution is bimodal at high redshifts.

local early-type galaxies (Young et al. 2011; Serra et al. 2011).

4.2. The role of cold and hot gas flows

We then turn our attention to studying how the gas is accreted onto the halos, where the accretion rate is defined as the gas mass flux through the virial radius at the corresponding redshift. Following the approach taken in Kereš et al. (2005, 2009) we study the maximum

temperature attained by accreted gas particles in order to deduce if they were accreted in a cold or hot mode. In Fig. 13 we show the maximum temperatures of all gas particles accreted since the previous snapshot, which corresponds to a physical timestep of $\Delta t \sim 300$ Myr at $z = 3, z = 5$ and $\Delta t \sim 700$ Myr at $z = 1, z = 0$. We record the maximum temperature of the accreted gas particles at all previous snapshots excluding the snapshots when the gas particles were starforming, in which

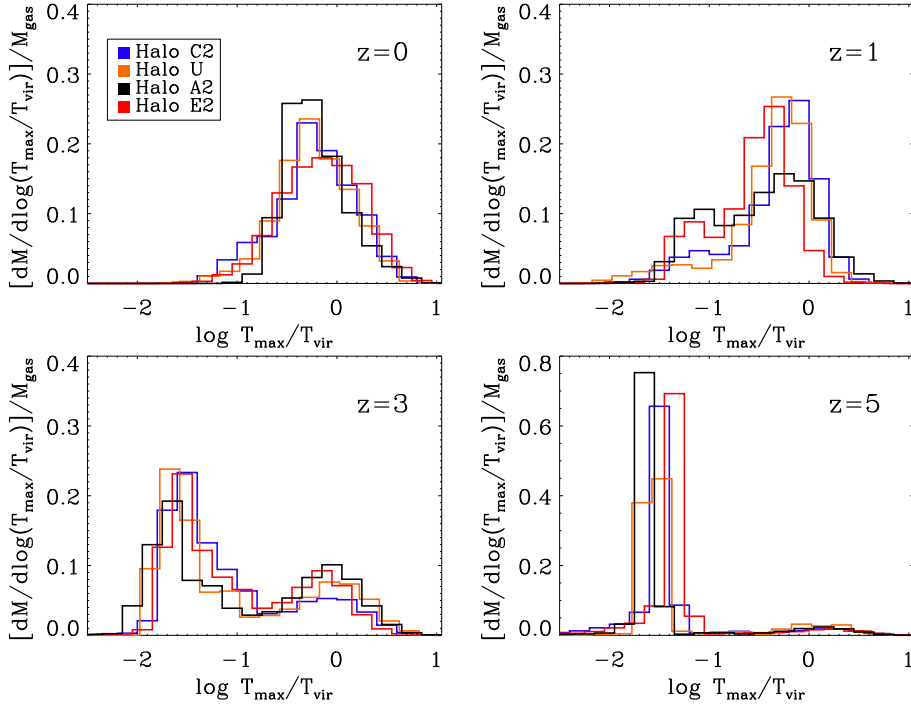


FIG. 13.— Distribution of the maximum past temperatures normalized to the virial temperature of gas accreting onto halos C2 (blue), U (orange), A2 (black), and halo E2 (red) as a function of redshift. At high redshifts the majority of gas is accreted cold, whereas at $z = 0$ the majority of the gas is accreted in a hot mode with $T \sim T_{\text{vir}}$.

case the high gas temperature was due to supernova feedback and not hydrodynamical processes. We then relate these maximum temperatures to the virial temperature of the halos at the time of accretion and plot the relative mass accretion rates as a function of $T_{\text{max}}/T_{\text{vir}}$ in Fig. 13.

Inspecting the figure one can see that virtually all of the accreted gas particles at $z = 5$ have temperatures below a tenth of the virial temperatures of the halos. Keeping in mind that the virial temperature at $z \sim 5$ is typically a few times 10^5 K this indicates that the gas is accreted in a cold phase with typical temperatures of a few times 10^4 K. At $z = 3$ the temperature distribution is more bimodal with the majority of the gas being accreted cold, but with a significant component of hot gas being accreted with $T \sim T_{\text{vir}}$. This coincides with an increase of hot halo gas and halo masses of $M_{\text{halo}} = 3 - 5 \times 10^{11} M_{\odot}$ (see Fig. 1). By $z \sim 1$ the majority of the gas is accreted in the hot phase with some residual cold accretion and by $z \sim 0$ the accretion of cold gas has all but disappeared. Thus the transition from a cold gas accretion mode to a hot gas accretion mode occurs at $z \sim 2 - 3$, corresponding to halo masses of $M_{\text{halo}} = 5 \times 10^{11} M_{\odot} - 10^{12} M_{\odot}$ in good agreement with the predictions of Dekel & Birnboim (2006), see also Rees & Ostriker (1977) and Silk (1977). Below these redshifts the galaxy halos are massive enough to support stable shocks and most of the accreted gas is shock-heated close to the virial temperature of the halos, whereas at higher redshifts the halos are not massive enough to support stable accretion shocks and most of the gas is accreted cold. This transition is also mass-

dependent, with an earlier transition occurring for more massive halos. Thus at $z \sim 3$ the more massive halos U, A2 have slightly larger fractions of hot gas than the lower mass halos C2, E2 (Fig 12), with also some differences in the hot gas fractions persisting until $z \sim 1$. At $z = 0$ the hot gas fractions are very high for all halos at $f_{\text{hot}} \gtrsim 97\%$, as most of the original gas has either formed stars or been shock-heated to very high temperatures.

To better illustrate the importance of cold/hot gas accretion we show in Fig. 14 the gas surface densities, together with the mass-weighted temperatures and entropies for the very high resolution halo A2 as a function of redshift. The images are generated by projecting the properties of the SPH particles through a physical slice of 100 kpc along the line-of-sight using the gather approximation (see Dolag et al. 2005) and binning the data over 256^2 pixels. The corresponding pixel resolutions are 0.39 kpc, 1.17 kpc, 2.44 kpc and 3.91 kpc for redshifts $z = 5, 3, 1$ and $z = 0$, respectively. The image resolution were chosen in order to resolve the virial radii drawn as solid circles at each redshift. At $z = 5$ the central galaxy is sitting at the intersection of gas filaments through which cold high-density gas is being fed into the galaxy (particularly well visible in the entropy plot as blue filaments). By $z = 3$ and especially $z = 1$ the amount of hot gas has increased significantly, however at both redshifts cold gas filaments are able to penetrate into the halo and feed the central gaseous structure where star formation takes place (see also Dekel et al. 2009a,b). The accretion of cold gas is clumpy producing turbulent eddies in the gas and at $z = 1$ even an elongated extended gaseous structure. By contrast the distribution

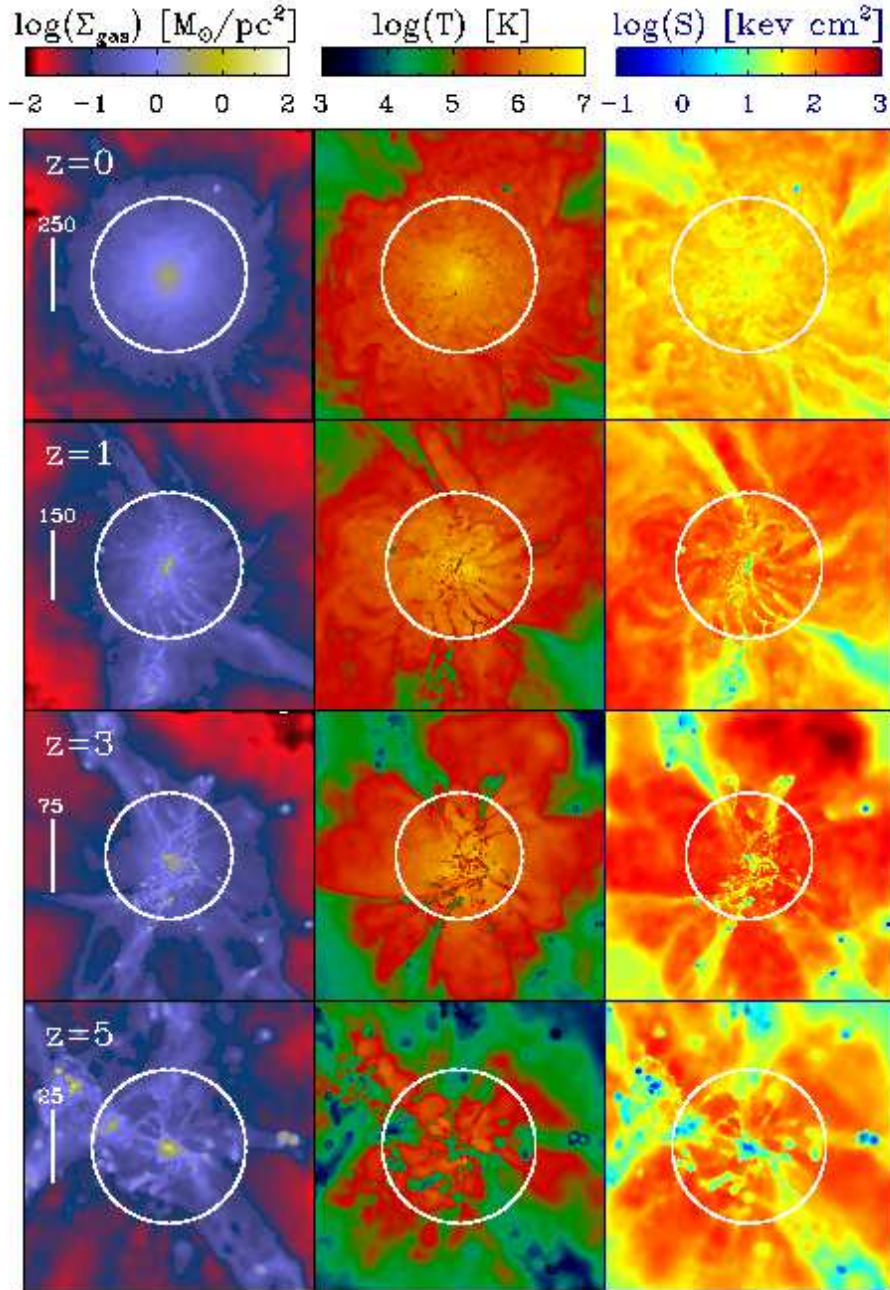


FIG. 14.— Evolution of gas surface density, Σ_{gas} (left panel), the mass-weighted mean gas temperature, T (middle panel) and the mass-weighted mean gas entropy, $S = kTn^{-2/3}$ (right panel) for the high resolution Halo A2 at redshifts $z = 0, z = 1, z = 3, z = 5$ from top to bottom. The length scale of each panel is depicted by the white bar in kpc, with each panel representing a slice with depth 100 kpc centered at the position of the central stellar component and binned with 256^2 pixels.

of gas at $z = 0$ is much smoother with almost the entire gas component found in a hot diffuse state with only very minor traces of cold clumpy gas remaining.

4.3. Gravitational heating of the gas component

Next we study the effect of gravitational feedback, which comes in many forms. Accreted lumps and streams of cold gas eventually come to rest due to drag forces depositing their potential energy frictionally (i.e. through

decaying turbulence, see e.g. Birnboim & Dekel 2011). Supersonic collisions of infalling gas with the ambient gas lead to propagating shock waves that deposit energy and entropy throughout the system (Ryu et al. 2003). And finally infalling satellite systems captured through dynamical friction cause gaseous wakes from which energy is transferred to the surrounding gas (Ostriker 1999).

Following the analysis presented in J09 we plot the cooling and heating rates for diffuse gas, i.e. non-

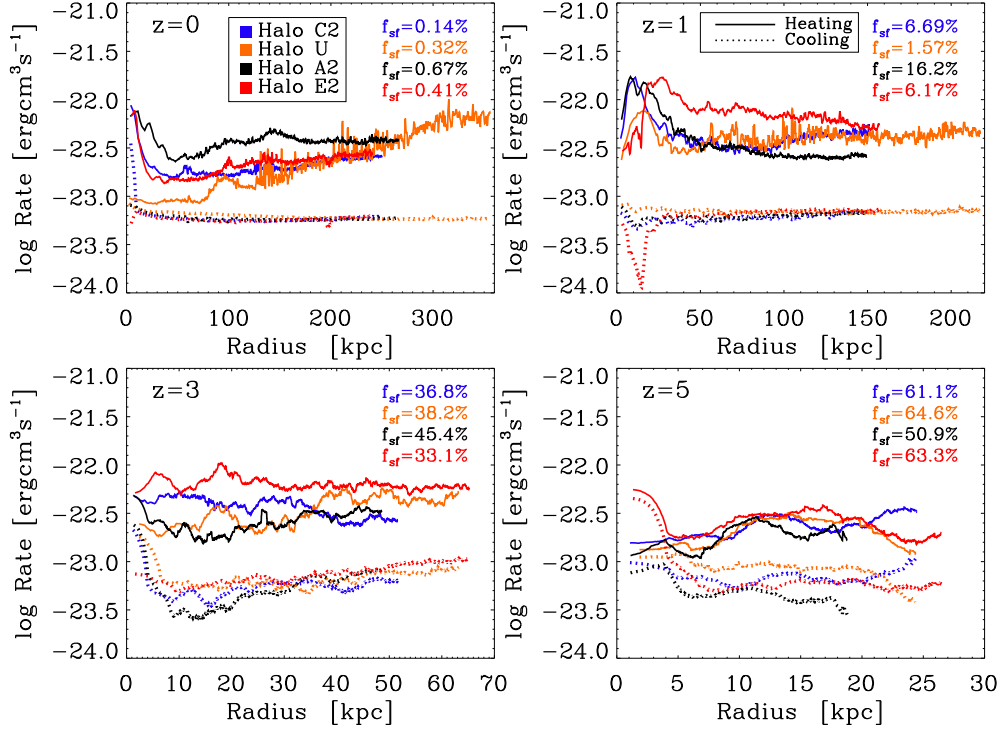


FIG. 15.— The net heating (solid line) and net cooling rates (dashed lines) for non-starforming ($\rho < \rho_{\text{thresh}}$) gas within the virial radius at redshifts 0, 1, 3 and 5 for the four halos. The fraction f_{sf} of dense starforming gas ($\rho > \rho_{\text{thresh}}$) is also given. Typically, the heating rate dominates over the cooling rate at all redshifts for the low-density non-starforming gas.

starforming gas with ($\rho < \rho_{\text{thresh}}$) in Fig. 15. The rates are estimated using the entropy equation in GADGET-2 which is for a given particle i (Springel & Hernquist 2002),

$$\frac{dA_i}{dt} = -\frac{\gamma-1}{\rho_i} \Lambda(\rho_i, u_i) + \frac{1}{2} \frac{\gamma-1}{\rho_i} \sum_{j=1}^N m_j \Pi_{ij} \mathbf{v}_{ij} \cdot \nabla_i \bar{W}_{ij}, \quad (7)$$

where the first term depicts the external radiative cooling (or heating) of the gas and the second term gives the generation of entropy by artificial viscosity in shocks and where the internal energy is defined as $u = A/(\gamma-1)\rho^{\gamma-1}$. The infalling clumps have typically velocities of $v \sim 100 - 400$ km/s, with the larger velocities corresponding to the galaxies at lower redshifts with larger potential wells. The corresponding sound speeds are a few factors lower, typically $c_s \sim 20 - 150$ km/s, thus giving rise to weak shocks with Mach numbers of 2-5. The gravitational feedback energy is then released in the weak shocks into the gas through dissipation of turbulence.

From Fig. 15 we see that a substantial fraction of the gas ($\sim 2/3$ at $z = 5$) and ($\sim 1/3$ at $z = 3$) is starforming, and at $z \sim 1$ the starforming gas fraction remains at $\sim 10\%$. Comparing this to the no feedback case presented in J09 we see that the starforming fractions at $z = 3 - 5$ are similar, whereas the feedback case shows starforming fractions higher by a factor of ~ 3 at $z = 1$ compared to the no feedback simulations. By $z = 0$ the starforming fraction is very low at $\lesssim 1\%$.

The shock-induced heating rates of the diffuse gas is larger than the cooling rates at all redshifts, thus explain-

ing the systematic increase in the diffuse gas temperature with decreasing redshift (Fig. 12). The absolute values of the heating rates in the present feedback simulations for a given halo are somewhat lower than the corresponding rates in the no feedback simulation, whereas the cooling rates are very similar in the two simulation samples. This indicates that the effect of gravitational heating in the simulations with supernova feedback is somewhat lower, as expected, due to the overall suppression of low-mass systems that could give rise to gravitational heating when accreted onto the main galaxy. According to analytical estimates presented in J09 the efficiency of gravitational feedback scales as $(\Delta E)_{\text{grav}} \propto v_c^2$, where v_c is the circular velocity of the galaxy. Thus gravitational heating should be stronger in more massive systems, which can also be seen in the $z = 0$ panel of Fig. 15, the more massive halos U and A2 show heating rates above those of the somewhat lower mass halos C2 and E2. An additional factor which needs to be taken into account when comparing halo U to halos A2, C2 and E2 is the fact that the latter simulations have higher numerical resolution and are expected to show larger gravitational heating rates. At higher resolution smaller mass clumps can be better resolved and thus the gravitational heating rates at higher resolution are systematically higher as was shown in the resolution study presented in J09.

An interesting case is the most massive halo U, which at $z = 0$ show very high heating rates in the outer parts of the halo, with the heating rate dropping by an order of magnitude towards the central parts of the galaxy. This galaxy possesses a very extended hot gaseous halo and

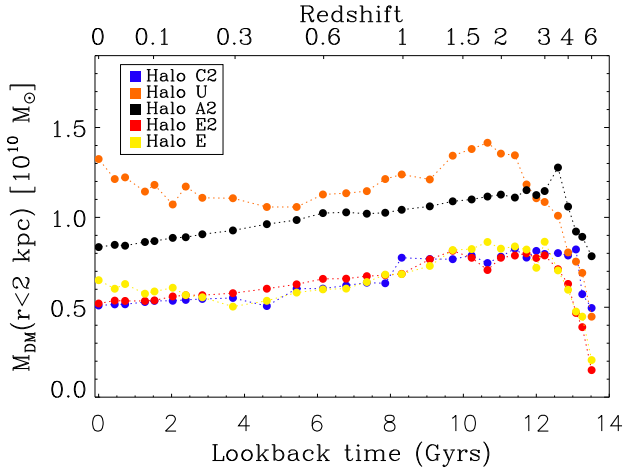


FIG. 16.— Cumulative DM mass distribution within $r < 2$ kpc as a function of lookback time (redshift) for halos C2,U,A2,E2 and E. Typically the central DM mass peaks at $z \sim 2 - 3$ after which it somewhat declines until $z = 0$.

our results imply that most of the gravitational energy is deposited at large radii $r > 100$ kpc outside the central galaxy. Thus, for the most massive galaxies (U,Y) in our sample gravitational heating alone is not strong enough to overcome the cooling in the central parts of the galaxies at late times ($z \lesssim 0.5$) at which time most of the accretion process is over. Consequently these galaxies experience strong late gas inflows as seen in Fig. 2, which also results in some residual star formation at $z = 0$ (see Table 2). The natural candidate for inhibiting these late gas inflows and residual star formation is the feedback from a supermassive black hole (e.g. Ciotti et al. 2009; Ostriker et al. 2010). Thus, we conclude that although gravitational feedback is important in keeping diffuse gas hot, especially in the outer parts of the galactic haloes, some form of additional feedback, most probably AGN feedback, is required to stop late central star formation in the more massive galaxies.

4.4. Gravitational heating of the DM component

The typical dark matter fractions within the virial radii in our simulated galaxies are $\sim 5/6$ indicating at the same time that the majority of the available baryons are retained within the virial radius of our simulated galaxies and that dark matter is the dominant mass component within the virial radius. The gravitational energy input scales with the mass fraction of each component, thus in addition to heating the baryonic gas component we expect that a fraction $\Omega_m/(\Omega_m + \Omega_b) = 5/6$ of the available feedback energy goes into heating the DM component. The feedback energy is deposited into the system through dynamical friction from infalling clumps that pushes out the existing stellar and dark matter components reducing the central densities (J09). Calculations which assume adiabatic contraction of the dark matter component and ignore the effect of gravitational heating tend to overestimate the central dark matter densities.

In Fig. 16 we quantify this effect by plotting the central DM mass within $r < 2$ kpc in our four galaxies (circles) as a function of lookback time. Initially we see an increase in the central DM due to adiabatic contraction (Blumenthal et al. 1986; Gnedin et al. 2004) for all the

galaxies with a peak central DM mass reached at $z \sim 3$. After the peak DM mass has been reached the central DM mass steadily declines due to the gravitational heating of infalling clumps. The relative change in the central DM mass between the peak at $z \sim 3$ and the final value at $z = 0$ is proportional to the amount of gravitational heating and thus to the amount of accreted stars. Thus this effect should be strongest for halos U and C2, followed by A2 and E2 in decreasing order. Indeed, we find that the central DM masses of the halos between the peak at $z \sim 3$ and $z = 0$ are reduced by 38% for halo C2, 35% for halo A2 and 33% for halo E2. The picture is more complicated for halo U, the DM in this system first experiences adiabatic contraction at $z \sim 3$, followed by a gravitational heating induced expansion phase where the central DM is reduced and then at late times a second adiabatic contraction phase induced by the late inflow of gas and associated star formation at $z \lesssim 0.5$, thus explaining the late upturn in the central DM mass. We note that the overall relative expansions of the central dark matter between $z = 3$ and $z = 0$ are lower by factors of ~ 2 when compared to the no feedback simulations in J09, for which the central DM was typically reduced by 60% between $z \sim 3$ and $z = 0$. This again demonstrates the reduced importance of gravitational feedback in simulations that include supernova feedback and most importantly that gravitational feedback is now not able to completely negate the effect of adiabatic contraction. The final central DM mass of halo A2 is higher by a factor of two compared to the corresponding final central DM mass of the DM only simulation presented in J09. Thus, in all our simulations including supernova feedback we see the effects of adiabatic contraction in better agreement with the recent study of Gnedin et al. (2011). Finally, we also show in Fig. 16 the evolution of the central dark matter mass of galaxy E at 100^3 resolution, which agrees well with the evolution of galaxy E2 at 200^3 resolution and thus demonstrates that the late reduction of the central dark matter densities is not due to numerical two-body relaxation effects (e.g. Diemand et al. 2004).

The ability of gravitational feedback to lower the central DM masses has important implications for the recent estimates of central dark matter content of elliptical galaxies (e.g. Thomas et al. 2009). Traditionally there has been some tension in the standard CDM model between numerical simulations that predict cuspy dark matter profiles (e.g. Moore et al. 1999 and the observations that indicate that many galaxies have finite dark matter cores (e.g. Gentile et al. 2004). As demonstrated in Fig. 10 (see also El-Zant et al. 2001; Ma & Boylan-Kolchin 2004; Romano-Díaz et al. 2008, 2009) the gravitational energy release from infalling clumps might help in transforming an initially cuspy DM profile into a more cored profile, although additional sources not included in this study, such as strong wind-driven supernova feedback (e.g. Pontzen & Governato 2011; Governato et al. 2012) and AGN feedback are probably also required to prevent late gas inflows and the associated excessive adiabatic contraction.

5. DISCUSSION

In this first paper of our two paper series we have explored in detail the assembly histories of massive elliptical

cals by performing a suite of high resolution simulations starting from cosmological initial conditions. Our simulations include primordial cooling, star formation and feedback from type II supernovae, but exclude supernova driven winds and AGN feedback. However, we stress that our simplified treatment does include, automatically, the important mechanism of gravitational heating which is often neglected in semi-analytic treatments but is a quite important aspect of maintaining overall energy conservation. Thus, the purpose of this paper was to see what aspects of the problems of the formation of massive galaxies could be addressed without invoking major feedback mechanisms and to see if a careful and high resolution treatment from cosmological initial conditions would capture the essential aspects of the formation process. In a companion paper (Paper II Johansson et al. in prep) we will study the photometric and kinematic properties of our simulated galaxies and compare the results with recent observations of early-type galaxies.

In agreement with our previous studies (N07; J09; Oser et al. 2010, 2012) we find that there are two phases in the formation process of our simulated galaxies. The initial growth is dominated by compact ($r < r_{\text{eff}}$) in situ star formation fueled by cold gas flow resulting in early star formation peaking at very high values of $\sim 50 - 120 M_{\odot}/\text{yr}$ at redshifts of $z \sim 4 - 5$. The later formation history below redshifts of $z \lesssim 2$ is dominated by dissipationless accretion of stars formed in subunits outside the main galaxy and the corresponding star formation rates are much lower with typical SFR values of $\lesssim 1 M_{\odot}/\text{yr}$. The accreted stars assemble predominantly at larger radii ($r > r_{\text{eff}}$) explaining both the size and mass growth of the simulated galaxies in broad agreement with the observations.

We also find a relation between the mass of the system and the fraction of accreted stars in the final galaxy, the larger the mass of the final galaxy the higher the fraction of accreted stars. This being the general picture, differences between the simulated galaxies exist even within a similar mass range caused by variations in the individual accretion histories of the various galaxies. We also find that gravitational heating due to infalling baryonic lumps of stars and gas is a major physical process that typically releases of the order of $\sim 10^{60}$ ergs (J09) of which about $1/6$ ($\Omega_b/(\Omega_m + \Omega_b) = 1/6$) goes to the gas and $5/6$ to the dark matter, heating the former and pushing out the latter. The combined effect of gas exhaustion due to early efficient star formation and the energy release from gravitational feedback terminates star formation in most galaxies by $z = 2$, resulting in dead and red ellipticals by $z = 1$ in good agreement with the observations.

The three main recent observational results concerning early-type galaxies are firstly the observed bimodality in the local galaxy population that postulates that galaxies below a critical stellar mass of $M_{\text{crit}} \simeq 3 \times 10^{10} M_{\odot}$ are typically blue, star-forming disk galaxies that lie in the field, whereas galaxies above M_{crit} are dominated by red spheroidal systems with old stellar populations that predominately live in dense environments (e.g. Kauffmann et al. 2003; Baldry et al. 2004). Secondly, there is now very strong observational evidence that old, massive red metal-rich galaxies were already at place at redshifts of $z=2-3$ and that the most massive galaxies formed a significant proportion of their

stars at high redshifts (e.g. Brinchmann & Ellis 2000; van der Wel et al. 2005). Thirdly, recent observations have revealed growth in both the size (e.g. Trujillo et al. 2007; van Dokkum et al. 2008) and mass (e.g. Bell et al. 2004; Faber et al. 2007) of massive ellipticals since $z=2-3$ until the present-day.

The two-phase formation for elliptical galaxies presented in this paper naturally explains all of these observations. In our simulations the central parts of the galaxies form very rapidly at high redshifts through cold accretion driven in situ star formation. The more massive galaxies which are located in higher density regions assemble first, the later formation history of these massive galaxies is then dominated by accretion of stars that were formed in smaller subunits at even earlier times. Thus, the more massive a galaxy is the earlier it formed and the older its average stellar population is due to the larger fraction of accreted stars thus explaining the downsizing observations. In our scenario the observed bimodality can be explained by the combined effect of gas exhaustion due to early star formation and gravitational feedback. In more massive galaxies the fraction of accreted stars is higher leading to stronger gravitational feedback heating and resulting in stronger suppression of star formation. Less massive galaxies have more ongoing in situ star formation and thus remain bluer throughout.

Gravitational feedback is thus a contributing factor in explaining the galaxy bimodality, but also additional heating sources probably in the form of strong supernova driven winds and AGN feedback are required to prevent late gas inflows and associated residual star formation. Additionally, the observed size growth of ellipticals is quite naturally explained in our model, in which dry minor mergers are responsible for the size growth, with the most massive galaxies showing the strongest growth in size as they have the largest fraction of accreted stars (see also Naab et al. 2009; Oser et al. 2010, 2012). Finally, we are able to match reasonably well the observational constraints on the central dark matter fractions of early-type galaxies at the present-day. In the two-phased formation picture the forming galaxies are strongly baryon dominated at high redshifts with correspondingly low dark matter fractions and very steep total density profiles ($\gamma' = -d \log \rho_{\text{tot}} / d \log r$). At lower redshifts the central dark matter fractions increase, although the total dark matter masses within $r < 2$ kpc are at the same time somewhat reduced due to the input of gravitational heating. At the present-day our simulated galaxies have central dark matter fractions of $f_{\text{DM}} \sim 0.1 - 0.3$, with the logarithmic slope of the total density profile being in the range $\gamma' \sim 1.9 - 2.2$ in good agreement with recent observations (Koopmans et al. 2006; Auger et al. 2009, 2010).

We also want to stress the importance of numerical resolution in galaxy formation studies. When comparing our simulation runs at 200^3 resolution (A2,C2,E2) to their corresponding runs at 100^3 resolution (A,C,E), we see some systematic effects. The final stellar masses in the higher resolution runs are typically lower by $\sim 10 - 20\%$ and as a result the rotation curves for the 200^3 runs peak at values that are $\sim 20 - 40$ km/s lower than their corresponding 100^3 runs with the overall shape also being flatter (see Fig 7). More importantly the final star formation rates of all the 200^3 resolution are very low

(SFR $\sim 0.3 - 0.4 M_{\odot}/\text{yr}$), with the corresponding 100^3 resolution simulations having star formation rates that are typically larger by $\sim 50\%$. Resolution has a more minor effect on the baryonic conversion efficiency, as the somewhat lower stellar masses in the high-resolution simulations also correspondingly reside in somewhat lower mass DM halos. The derived differences are mainly due to the increased input of gravitational heating with increasing resolution, but comparing to the no feedback simulations discussed in N07;J09 we see that the sensitivity to numerical resolution, although still there, is significantly reduced in simulations that include supernova feedback. Thus in conclusion, it is important to perform the cosmological simulations at both sufficient mass ($\lesssim 10^5 M_{\odot}$) and spatial resolution (~ 0.1 kpc) (see also Governato et al. 2010; Guedes et al. 2011 for very high resolution simulations of lower mass disk galaxies).

Despite the many successes of our simple model several problems still remain. The most pressing issue is the fact that the fractions of available baryons in the halo that is converted into stars in the central galaxy are too high by a factor of ~ 2 compared to the expectation from halo occupation statistics (Guo et al. 2010; Moster et al. 2010) and to some recent simulations with stronger supernova feedback (Governato et al. 2010; Guedes et al. 2011). In addition the final gas fractions and resulting star formation rates while generally low are still somewhat too large, especially for the more massive galaxies in our simulation sample.

A major deficiency of our simulations is the lack of metal-line cooling. Assuming solar metallicities expected in intermediate-mass early-type galaxies and the temperatures of $T = 10^5 - 10^6$ K depicted in Fig. 15 would result in cooling rates that were higher by at least one order of magnitude (Sutherland & Dopita 1993) bringing them much closer to the inferred shock heating rates and thus limiting the ability of gravitational feedback to keep the diffuse halo hot. According to the mass-metallicity relation (e.g. Finlator & Davé 2008) the most massive galaxies have on average the highest metallicities. Thus the fact that gravitational feedback is unable to prevent cooling in our most massive galaxies U & Y even at zero-metallicity is a very strong indication that additional forms of feedback, such as AGN feedback is required in massive metal-rich galaxies. The inclusion of metal-line cooling would also impact the in situ and accreted analysis differentially as the centers of the massive galaxies where the in situ stellar component is formed would have higher metallicities resulting in stronger cooling and star formation, thus increasing the final in situ to accreted stellar mass fraction in our galaxies. Consequently the already severe problem of too high baryon fractions would be made even more critical. Thus, it is clear from the discussion above that just adding metal-line cooling keeping everything else fixed would have a large effect on the results presented in this paper. Specifically, the in situ stellar component would be increased reducing the effect of the accreted stellar component in driving the size growth of the galaxies, the central concentrations of our galaxies would increase making the central baryon fractions even larger and finally the increased cooling would reduce the effects of the gravitational feedback making the case for additional AGN feedback in the centers of massive metal-rich galaxies even

more pressing.

However, adding just metal-line cooling, without adding the additional heating mechanisms, which to some respect offset the increased cooling would not result in a fair presentation of the underlying baryonic physics. Thus the simultaneous exclusion of both metal-line cooling and strong additional feedback is better justified in this simple model than just including metal-line cooling without the additional feedback physics. In addition to metal-line cooling we are missing important physical effects such as stellar mass loss (e.g. Schaye et al. 2010; Leitner & Kravtsov 2011) and in addition several important heating sources including AGN feedback from broad absorption line wind regions and the luminous AGN radiative output (e.g. Sazonov et al. 2004; Johansson et al. 2009b; Booth & Schaye 2009; Schaye et al. 2010; Debuhr et al. 2010; Ostriker et al. 2010), radiative driven winds from the coupling with the luminous output of young stars (e.g. Oppenheimer & Davé 2006; Petkova & Springel 2009; Hopkins et al. 2011) and feedback from type Ia supernovae (e.g. Scannapieco et al. 2005; Ciotti & Ostriker 2007; Oppenheimer & Davé 2008) in addition to the simplified prescription of type II supernova feedback currently included in the simulations.

The effect of supernova driven winds and AGN feedback is differential with respect to the masses of the galaxies, the former is most important for low-mass galaxies, whereas the latter being only important in more massive galaxies. We expect that the problem with the too high baryonic conversion efficiency will be mainly addressed by adding stronger supernova driven winds, whereas the problem of residual star formation in massive galaxies is best addressed by adding AGN feedback and type I supernova that are both mostly effective in the cores of massive galaxies. An additional factor for suppressing late star formation would be simply increasing the numerical resolution of the simulation as clearly demonstrated in N07. We have completed preliminary work including strong supernova wind feedback (Genel et al. 2012) and AGN feedback (Hambrick et al. 2011b) and find that the addition of both of these effects can plausibly solve the problems encountered in the present simulations. Thus, although the inclusion of all these feedback effects would certainly lower the overall total stellar masses in accordance with the observations, the relative contribution of in situ and accreted stellar mass might not be significantly affected and thus the general picture of a two-phased formation mechanism presented in this paper would remain valid. The next test of our cosmological two-phased formation scenario would be the inclusion of the aforementioned additional feedback sources in very high resolution zoom-in simulations of galaxies spanning a much wider range in both mass and environmental density, with the ultimate goal remaining the simultaneous production of fully realistic elliptical and disk galaxies in the same simulation.

We thank the anonymous referee for a careful reading of the manuscript and valuable comments. In addition, we thank M. Cappellari, L. Ciotti, F. Governato, S. Leitner and F. Shankar for helpful comments on the manuscript. The numerical simulations were performed

at the Princeton PICSciE HPC center. PHJ acknowledges the support of the Research Funds of the University of Helsinki. TN acknowledges the support of the

DFG excellence cluster 'The origin and structure of the Universe and the DFG Priority Program 1177.

REFERENCES

- Abadi, M. G., Navarro, J. F., Steinmetz, M., & Eke, V. R. 2003, *ApJ*, 591, 499
- Agertz, O., Teyssier, R., & Moore, B. 2009, *MNRAS*, 397, L64
- Agertz, O., Teyssier, R., & Moore, B. 2011, *MNRAS*, 410, 1391
- Auger, M. W., Treu, T., Bolton, A. S., et al. 2009, *ApJ*, 705, 1099
- Auger, M. W., Treu, T., Bolton, A. S., et al. 2010, *ApJ*, 724, 511
- Baldry, I. K., Glazebrook, K., Brinkmann, J., Ivezić, Ž., Lupton, R. H., Nichol, R. C., & Szalay, A. S. 2004, *ApJ*, 600, 681
- Barnabè, M., Czoske, O., Koopmans, L. V. E., Treu, T., & Bolton, A. S. 2011, *MNRAS*, 415, 2215
- Barnabè, M., Czoske, O., Koopmans, L. V. E., Treu, T., Bolton, A. S., & Gavazzi, R. 2009, *MNRAS*, 399, 21
- Barnes, J. E. & Hernquist, L. 1996, *ApJ*, 471, 115
- Bell, E. F., McIntosh, D. H., Katz, N., & Weinberg, M. D. 2003, *ApJS*, 149, 289
- Bell, E. F., Naab, T., McIntosh, D. H., et al. 2006, *ApJ*, 640, 241
- Bell, E. F., Wolf, C., Meisenheimer, K., et al. 2004, *ApJ*, 608, 752
- Bezanson, R., van Dokkum, P. G., Tal, T., Marchesini, D., Kriek, M., Franx, M., & Coppi, P. 2009, *ApJ*, 697, 1290
- Binney, J. 1977, *ApJ*, 215, 483
- Birnboim, Y. & Dekel, A. 2003, *MNRAS*, 345, 349
- Birnboim, Y. & Dekel, A. 2011, *MNRAS*, 415, 2566
- Birnboim, Y., Dekel, A., & Neistein, E. 2007, *MNRAS*, 380, 339
- Blumenthal, G. R., Faber, S. M., Flores, R., & Primack, J. R. 1986, *ApJ*, 301, 27
- Bois, M., Bournaud, F., Emsellem, E., et al. 2010, *MNRAS*, 406, 2405
- Bois, M., Emsellem, E., Bournaud, F., et al. 2011, *MNRAS*, 416, 1654
- Bolton, A. S., Treu, T., Koopmans, L. V. E., et al. 2008, *ApJ*, 684, 248
- Booth, C. M. & Schaye, J. 2009, *MNRAS*, 398, 53
- Bournaud, F., Jog, C. J., & Combes, F. 2005, *A&A*, 437, 69
- Bower, R. G., Benson, A. J., Malbon, R., Helly, J. C., Frenk, C. S., Baugh, C. M., Cole, S., & Lacey, C. G. 2006, *MNRAS*, 370, 645
- Brinchmann, J. & Ellis, R. S. 2000, *ApJ*, 536, L77
- Brooks, A. M., Governato, F., Quinn, T., Brook, C. B., & Wadsley, J. 2009, *ApJ*, 694, 396
- Bullock, J. S., Dekel, A., Kolatt, T. S., Kravtsov, A. V., Klypin, A. A., Porciani, C., & Primack, J. R. 2001, *ApJ*, 555, 240
- Bundy, K., Ellis, R. S., Conselice, C. J., et al. 2006, *ApJ*, 651, 120
- Burkert, A., Naab, T., Johansson, P. H., & Jesseit, R. 2008, *ApJ*, 685, 897
- Cappellari, M., Emsellem, E., Bacon, R., et al. 2007, *MNRAS*, 379, 418
- Cappellari, M., Emsellem, E., Krajnović, D., et al. 2011, *MNRAS*, 413, 813
- Cattaneo, A., Dekel, A., Devriendt, J., Guiderdoni, B., & Blaizot, J. 2006, *MNRAS*, 370, 1651
- Cimatti, A., Cassata, P., Pozzetti, L., et al. 2008, *A&A*, 482, 21
- Cimatti, A., Daddi, E., & Renzini, A. 2006, *A&A*, 453, L29
- Ciotti, L. & Ostriker, J. P. 2007, *ApJ*, 665, 1038
- Ciotti, L., Ostriker, J. P., & Proga, D. 2009, *ApJ*, 699, 89
- Cocato, L., Gerhard, O., Arnaboldi, M., et al. 2009, *MNRAS*, 394, 1249
- Cole, S., Lacey, C. G., Baugh, C. M., & Frenk, C. S. 2000, *MNRAS*, 319, 168
- Cox, T. J., Dutta, S. N., Di Matteo, T., et al. 2006, *ApJ*, 650, 791
- Croton, D. J., Springel, V., White, S. D. M., et al. 2006, *MNRAS*, 365, 11
- Daddi, E., Renzini, A., Pirzkal, N., et al. 2005, *ApJ*, 626, 680
- Davé, R., Hernquist, L., Katz, N., & Weinberg, D. H. 1999, *ApJ*, 511, 521
- De Lucia, G., Springel, V., White, S. D. M., Croton, D., & Kauffmann, G. 2006, *MNRAS*, 366, 499
- Debuhr, J., Quataert, E., & Ma, C.-P. 2011, *MNRAS*, 2150
- Debuhr, J., Quataert, E., Ma, C.-P., & Hopkins, P. 2010, *MNRAS*, 406, L55
- Dekel, A. & Birnboim, Y. 2006, *MNRAS*, 368, 2
- Dekel, A. & Birnboim, Y. 2008, *MNRAS*, 383, 119
- Dekel, A., Birnboim, Y., Engel, G., et al. 2009a, *Nature*, 457, 451
- Dekel, A., Sari, R., & Ceverino, D. 2009b, *ApJ*, 703, 785
- Diemand, J., Moore, B., Stadel, J., Kazantzidis, S. 2004, *MNRAS*, 348, 977
- Dolag, K., Hansen, F. K., Roncarelli, M., & Moscardini, L. 2005, *MNRAS*, 363, 29
- Driver, S. P., Popescu, C. C., Tuffs, R. J., Liske, J., Graham, A. W., Allen, P. D., de Propris, R. 2007, *MNRAS*, 379, 1022
- Drory, N., Bender, R., Feulner, G., Hopp, U., Maraston, C., Snigula, J., & Hill, G. J. 2004, *ApJ*, 608, 742
- Dubois, Y., Devriendt, J., Slyz, A., & Teyssier, R. 2012, *MNRAS*, 2188
- Efstathiou, G., Bond, J. R., & White, S. D. M. 1992, *MNRAS*, 258, 1P
- Eggen, O. J., Lynden-Bell, D., & Sandage, A. R. 1962, *ApJ*, 136, 748
- El-Zant, A., Shlosman, I., & Hoffman, Y. 2001, *ApJ*, 560, 636
- Emsellem, E., Cappellari, M., Krajnović, D., et al. 2011, *MNRAS*, 414, 888
- Faber, S. M., Willmer, C. N. A., Wolf, C., et al. 2007, *ApJ*, 665, 265
- Fall, S. M. & Efstathiou, G. 1980, *MNRAS*, 193, 189
- Feldmann, R., Carollo, C. M., & Mayer, L. 2011, *ApJ*, 736, 88
- Feldmann, R., Carollo, C. M., Mayer, L., et al. 2010, *ApJ*, 709, 218
- Finlator, K. & Davé, R. 2008, *MNRAS*, 385, 2181
- Franx, M., van Dokkum, P. G., Schreiber, N. M. F., Wuyts, S., Labbé, I., & Toft, S. 2008, *ApJ*, 688, 770
- Fukugita, M., Hogan, C. J., & Peebles, P. J. E. 1998, *ApJ*, 503, 518
- Genel, S., Naab, T., Genzel, R., et al. 2012, *ApJ*, 745, 11
- Genile, G., Salucci, P., Klein, U., Vergani, D., & Kalberla, P. 2004, *MNRAS*, 351, 903
- Glazebrook, K., Abraham, R. G., McCarthy, P. J., et al. 2004, *Nature*, 430, 181
- Gnedin, O. Y., Ceverino, D., Gnedin, N. Y., Klypin, A. A., Kravtsov, A. V., Levine, R., Nagai, D., & Yepes, G. 2011, *arXiv:1108.5736*
- Gnedin, O. Y., Kravtsov, A. V., Klypin, A. A., & Nagai, D. 2004, *ApJ*, 616, 16
- Governato, F., Brook, C., Mayer, L., et al. 2010, *Nature*, 463, 203
- Governato, F., Mayer, L., Wadsley, J., et al. 2004, *ApJ*, 607, 688
- Governato, F., Willman, B., Mayer, L., et al. 2007, *MNRAS*, 374, 1479
- Governato, F., Zolotov, A., Pontzen, A., et al. 2012, *arXiv:1202.0554*
- Grillo, C. 2010, *ApJ*, 722, 779
- Grillo, C. & Gobat, R. 2010, *MNRAS*, 402, L67
- Guedes, J., Callegari, S., Madau, P., & Mayer, L. 2011, *ApJ*, 742, 76
- Guo, Q. & White, S. D. M., 2008, *MNRAS*, 384, 2
- Guo, Q., White, S. D. M., Li, C., & Boylan-Kolchin, M. 2010, *MNRAS*, 404, 1111
- Haardt, F. & Madau, P. 1996, *ApJ*, 461, 20
- Hambrick, D. C., Ostriker, J. P., Johansson, P. H., & Naab, T. 2011a, *MNRAS*, 413, 2421
- Hambrick, D. C., Ostriker, J. P., Naab, T., & Johansson, P. H. 2009, *ApJ*, 705, 1566
- Hambrick, D. C., Ostriker, J. P., Naab, T., & Johansson, P. H. 2011b, *ApJ*, 738, 16
- Hoffman, L., Cox, T. J., Dutta, S., & Hernquist, L. 2009, *ApJ*, 705, 920
- Hopkins, P. F., Bundy, K., Hernquist, L., & Ellis, R. S. 2007, *ApJ*, 659, 976
- Hopkins, P. F., Bundy, K., Hernquist, L., Wuyts, S., & Cox, T. J. 2010, *MNRAS*, 401, 1099
- Hopkins, P. F., Hernquist, L., Cox, T. J., Dutta, S. N., & Rothberg, B. 2008a, *ApJ*, 679, 156
- Hopkins, P. F., Hernquist, L., Cox, T. J., Keres, D., & Wuyts, S. 2009, *ApJ*, 691, 1424
- Hopkins, P. F., Hernquist, L., Cox, T. J., & Kereš, D. 2008b, *ApJS*, 175, 356
- Hopkins, P. F., Quataert, E., & Murray, N. 2011, *MNRAS*, 417, 950
- Hubble, E. P. 1926, *ApJ*, 64, 321

- Johansson, P. H., Burkert, A., & Naab, T. 2009a, *ApJ*, 707, L184
- Johansson, P. H. & Efstathiou, G. 2006, *MNRAS*, 371, 1519
- Johansson, P. H., Naab, T., & Burkert, A. 2009b, *ApJ*, 690, 802
- Johansson, P. H., Naab, T., & Ostriker, J. P. 2009c, *ApJ*, 697, L38
- Joung, M. R., Cen, R., & Bryan, G. L. 2009, *ApJ*, 692, L1
- Juneau, S., Glazebrook, K., Crampton, D., et al. 2005, *ApJ*, 619, L135
- Katz, N., Weinberg, D. H., & Hernquist, L. 1996, *ApJS*, 105, 19
- Katz, N. & White, S. D. M. 1993, *ApJ*, 412, 455
- Kauffmann, G., Heckman, T. M., White, S. D. M., et al. 2003, *MNRAS*, 341, 33
- Kauffmann, G., White, S. D. M., & Guiderdoni, B. 1993, *MNRAS*, 264, 201
- Kennicutt, Jr., R. C. 1998, *ARA&A*, 36, 189
- Kereš, D., Katz, N., Fardal, M., Davé, R., & Weinberg, D. H. 2009, *MNRAS*, 395, 160
- Kereš, D., Katz, N., Weinberg, D. H., & Davé, R. 2005, *MNRAS*, 363, 2
- Khalatyan, A., Cattaneo, A., Schramm, M., Gottlöber, S., Steinmetz, M., & Wisotzki, L. 2008, *MNRAS*, 387, 13
- Khochfar, S. & Ostriker, J. P. 2008, *ApJ*, 680, 54
- Khochfar, S. & Silk, J. 2009, *MNRAS*, 397, 506
- Koopmans, L. V. E., Treu, T., Bolton, A. S., Burles, S., & Moustakas, L. A. 2006, *ApJ*, 649, 599
- Kormendy, J., Fisher, D. B., Cornell, M. E., & Bender, R. 2009, *ApJS*, 182, 216
- Krajinović, D., Emsellem, E., Cappellari, et al. 2011, *MNRAS*, 414, 2923
- Larson, R. B. 1975, *MNRAS*, 173, 671
- Leier, D., Ferreras, I., Saha, P., Falco, E. E., 2011, *ApJ*, 740, 97
- Leitner, S. N. & Kravtsov, A. V. 2011, *ApJ*, 734, 48
- Ma, C.-P. & Boylan-Kolchin, M. 2004, *Phys.Rev.Lett.*, 93, 1301
- Macciò, A. V., Dutton, A. A., van den Bosch, F. C., Moore, B., Potter, D., & Stadel, J. 2007, *MNRAS*, 378, 55
- Mandelbaum, R., Seljak, U., Kauffmann, G., Hirata, C. M., & Brinkmann, J. 2006, *MNRAS*, 368, 715
- McCarthy, I. G., Schaye, J., Ponman, T. J., et al. 2010, *MNRAS*, 406, 822
- McKee, C. F. & Ostriker, J. P. 1977, *ApJ*, 218, 148
- Meza, A., Navarro, J. F., Steinmetz, M., & Eke, V. R. 2003, *ApJ*, 590, 619
- Mihos, J. C. & Hernquist, L. 1994, *ApJ*, 431, L9
- Mihos, J. C. & Hernquist, L. 1996, *ApJ*, 464, 641
- Monaghan, J. J. 1992, *ARA&A*, 30, 543
- Moore, B., Quinn, T., Governato, F., Stadel, J., & Lake, G. 1999, *MNRAS*, 310, 1147
- Moster, B. P., Somerville, R. S., Maulbetsch, C., van den Bosch, F. C., Macciò, A. V., Naab, T., & Oser, L. 2010, *ApJ*, 710, 903
- Naab, T. & Burkert, A. 2003, *ApJ*, 597, 893
- Naab, T., Jesseit, R., & Burkert, A. 2006a, *MNRAS*, 372, 839
- Naab, T., Johansson, P. H., & Ostriker, J. P. 2009, *ApJ*, 699, L178
- Naab, T., Johansson, P. H., Ostriker, J. P., & Efstathiou, G. 2007, *ApJ*, 658, 710
- Naab, T., Khochfar, S., & Burkert, A. 2006b, *ApJ*, 636, L81
- Naab, T. & Ostriker, J. P. 2009, *ApJ*, 690, 1452
- Napolitano, N. R., Romanowsky, A. J., Coccato, L., et al. 2009, *MNRAS*, 393, 329
- Napolitano, N. R., Romanowsky, A. J., Capaccioli, M., et al. 2011, *MNRAS*, 411, 2035
- Ocvirk, P., Pichon, C., & Teyssier, R. 2008, *MNRAS*, 390, 1326
- Oppenheimer, B. D. & Davé, R. 2006, *MNRAS*, 373, 1265
- Oppenheimer, B. D. & Davé, R. 2008, *MNRAS*, 387, 577
- Oser, L., Naab, T., Ostriker, J. P., & Johansson, P. H. 2012, *ApJ*, 744, 63
- Oser, L., Ostriker, J. P., Naab, T., Johansson, P. H., & Burkert, A. 2010, *ApJ*, 725, 2312
- Ostriker, E. C. 1999, *ApJ*, 513, 252
- Ostriker, J. P., Choi, E., Ciotti, L., Novak, G. S., & Proga, D. 2010, *ApJ*, 722, 642
- Petkova, M. & Springel, V. 2009, *MNRAS*, 396, 1383
- Piontek, F. & Steinmetz, M. 2011, *MNRAS*, 410, 2625
- Pontzen, A. & Governato, F. 2011, arXiv:1106.0499
- Rees, M. J. & Ostriker, J. P. 1977, *MNRAS*, 179, 541
- Robertson, B., Yoshida, N., Springel, V., & Hernquist, L. 2004, *ApJ*, 606, 32
- Romano-Díaz, E., Shlosman, I., Heller, C., & Hoffman, Y. 2009, *ApJ*, 702, 1250
- Romano-Díaz, E., Shlosman, I., Hoffman, Y., & Heller, C. 2008, *ApJ*, 685, L105
- Ryu, D., Kang, H., Hallman, E., & Jones, T. W. 2003, *ApJ*, 593, 599
- Salpeter, E. E. 1955, *ApJ*, 121, 161
- Sazonov, S. Y., Ostriker, J. P., & Sunyaev, R. A. 2004, *MNRAS*, 347, 144
- Scannapieco, C., Tissera, P. B., White, S. D. M., & Springel, V. 2005, *MNRAS*, 364, 552
- Scannapieco, C., White, S. D. M., Springel, V., & Tissera, P. B. 2009, *MNRAS*, 396, 696
- Scannapieco, E. & Oh, S. P. 2004, *ApJ*, 608, 62
- Schaye, J., Dalla Vecchia, C., Booth, C. M., et al. 2010, *MNRAS*, 402, 1536
- Serra, P., Oosterloo, T., Morganti, R., et al. 2011, arXiv:1111.4241
- Shankar, F., Marulli, F., Bernardi, M., Mei, S., Meert, A., Vikram, V., 2011, arXiv:1105.6043
- Silk, J. 1977, *ApJ*, 211, 638
- Somerville, R. S., Hopkins, P. F., Cox, T. J., Robertson, B. E., & Hernquist, L. 2008, *MNRAS*, 391, 481
- Sommer-Larsen, J., Götz, M., & Portinari, L. 2003, *ApJ*, 596, 47
- Spergel, D. N., Verde, L., Peiris, H. V., et al. 2003, *ApJS*, 148, 175
- Springel, V. 2000, *MNRAS*, 312, 859
- Springel, V. 2005, *MNRAS*, 364, 1105
- Springel, V., Di Matteo, T., & Hernquist, L. 2005, *ApJ*, 620, L79
- Springel, V. & Hernquist, L. 2002, *MNRAS*, 333, 649
- Springel, V. & Hernquist, L. 2003, *MNRAS*, 339, 289
- Sutherland, R. S. & Dopita, M. A., 1993, *ApJS*, 88, 253
- Teyssier, R., Moore, B., Martizzi, D., Dubois, Y., & Mayer, L. 2011, *MNRAS*, 414, 195
- Theuns, T., Leonard, A., Efstathiou, G., Pearce, F. R., & Thomas, P. A. 1998, *MNRAS*, 301, 478
- Thomas, D., Maraston, C., Bender, R., & Mendes de Oliveira, C. 2005, *ApJ*, 621, 673
- Thomas, J., Saglia, R. P., Bender, R., Thomas, D., Gebhardt, K., Magorrian, J., Corsini, E. M., & Wegner, G. 2009, *ApJ*, 691, 770
- Trujillo, I., Conselice, C. J., Bundy, K., Cooper, M. C., Eisenhardt, P., & Ellis, R. S. 2007, *MNRAS*, 382, 109
- Trujillo, I., Förster Schreiber, N. M., Rudnick, G., et al. 2006, *ApJ*, 650, 18
- van Albada, T. S. 1982, *MNRAS*, 201, 939
- van der Wel, A., Bell, E. F., van den Bosch, F. C., Gallazzi, A., & Rix, H. 2009, *ApJ*, 698, 1232
- van der Wel, A., Franx, M., van Dokkum, P. G., Rix, H., Illingworth, G. D., & Rosati, P. 2005, *ApJ*, 631, 145
- van Dokkum, P. G. 2005, *AJ*, 130, 2647
- van Dokkum, P. G., Franx, M., Kriek, M., et al. 2008, *ApJ*, 677, L5
- van Dokkum, P. G., Kriek, M., & Franx, M. 2009, *Nature*, 460, 717
- van Dokkum, P. G., Whitaker, K. E., Brammer, G., et al. 2010, *ApJ*, 709, 1018
- Vitvitska, M., Klypin, A. A., Kravtsov, A. V., Wechsler, R. H., Primack, J. R., & Bullock, J. S. 2002, *ApJ*, 581, 799
- Weil, M. L., Eke, V. R., & Efstathiou, G. 1998, *MNRAS*, 300, 773
- White, S. D. M. & Frenk, C. S. 1991, *ApJ*, 379, 52
- White, S. D. M. & Rees, M. J. 1978, *MNRAS*, 183, 341
- Williams, R. J., Quadri, R. F., Franx, M., van Dokkum, P., & Labbé, I. 2009, *ApJ*, 691, 1879
- Wuyts, S., Cox, T. J., Hayward, C. C., et al. 2010, *ApJ*, 722, 1666
- Yang, X., Mo, H. J., van den Bosch, F. C., Zhang, Y., Han, J. 2011, arXiv:1110.1420
- Young, L. M., Bureau, M., Davis, T. A., et al. 2011, *MNRAS*, 414, 940